

# Chapter 7

## Comparison Between Neoclassical Modeling and Experimental Results

### 7.0 Introduction

Previous chapters have laid down the necessary pieces for a comparison between measurements of the plasma response to electrode bias and neoclassical predictions. In Chapter 4, detailed examples of the flow and floating potential evolution were provided, and data analysis methods were illustrated. Chapter 5 presented the details of the calculation of the Hamada coordinate magnetic field spectrum and basis vectors. Chapter 6 illustrated the neoclassical modeling techniques, including solutions for the time evolution and steady state values of the electric field and plasma flows. The current chapter presents comparisons between the measurements in Chapter 4 and the modeling in Chapters 5 and 6.

The modeling and data are naturally separated into the steady state solutions, the spin-up/electric field rise solutions, and the spin-down/electric field decay solution. This will be the ordering of this chapter. The comparisons will generally concentrate first on the QHS configuration; data and comparisons for the Mirror configuration will be discussed after the QHS comparison in many cases.

Section 1 will present the comparison between the steady state solutions of the neoclassical fluid equations and the fully evolved flow and electric field measurements. The radial profile of the radial conductivity will be the first subject, followed by its density scaling. These quantities will be discussed for both the QHS and Mirror configurations, and comparisons with neoclassical modeling and a model by Rozhansky and Tendler<sup>1</sup> will be discussed. These discussions will show that the radial conductivity in HSX appears to be anomalous. The next comparison in this section will deal with the predicted and modeled steady state flow direction.

The final comparison will be of the radial conductivity in hydrogen and deuterium discharges, where it will be shown that the  $m_i^{1/2}$  scaling of the radial conductivity in the modeling also appears in the data.

Section 2 deals with the spin-up of the plasma flow and formation of the electric field. Both the radial profile and density scaling of the "hybrid" time scale ( $\nu_F$ ) will be shown to be consistent with the measurements. This will be the case for both the QHS and Mirror configurations, providing the strongest evidence in this work that the QHS configuration has reduced neoclassical viscous damping compared to the Mirror configuration. A discussion of the directions associated with the fast and slow flow rise ends this section.

Section 3 presents a comparison between the measured and modeled relaxation of the flows and potentials. The modeling discussed in Chapter 6 showed that there is a fast and slow time scale associated with the neoclassical decays of the plasma flows and electric field. The measured decays of the floating potential and the fast component of the flow occur on a time scale which agrees with the neoclassical fast time scale. The slow component of the flow decay is much faster than the neoclassical prediction. The directions associated with the fast and slow decay differ from the neoclassical predictions.

Given the length of the chapter and the amount of data presented, it may be useful to state up front the most broad conclusions which have been drawn from these results. Phenomena associated with the neoclassical fast time scales, such as the damping of flows across the direction of symmetry, seem to be described reasonably well by neoclassical theory. Phenomena which have a strong dependence on the damping in the symmetry direction, such as the slow neoclassical time scale and the radial conductivity, are not well described by neoclassical theory.

## 7.1 Radial Conductivity Comparisons and the Steady State Plasma Flow Direction.

This section describes the measurements and modeling of the steady state biased plasma. The section is divided into four subsections. The first section provides information on the radial profile of the radial conductivity, followed by a section describing its density scaling. These sections will make comparisons between the measurements and modeling, including the extensive neoclassical modeling presented in this work and the modeling by Rozhansky and Tendler. The next section will provide a comparison between the measured and modeled steady state flow direction. The final section will examine the differences in radial conductivity between hydrogen and deuterium discharges.

### 7.1.1: Radial Conductivity Profiles

As described in Chapter 6, the radial conductivity describes the relationship between the plasma radial electric field and the current flowing across the magnetic surfaces:

$$\langle \mathbf{J} \cdot \nabla \psi \rangle = \sigma_{\perp} \left( -\langle \mathbf{E}_r \cdot \nabla \psi \rangle + \frac{\langle \nabla p_i \cdot \nabla \psi \rangle}{eN_i} \right). \quad (7.1)$$

The methods and tools for calculating the neoclassical  $\sigma_{\perp}$  are given in Chapters 5 & 6.

Consider first the solution of this equation before the biased electrode is energized. In the absence of a radial current, equation 7.1 implies

$$\langle \mathbf{E}_r \cdot \nabla \psi \rangle = \frac{\langle \nabla p_i \cdot \nabla \psi \rangle}{eN_i} \quad (7.2)$$

The experimental data shows that both the electric potential and plasma pressure increase towards the core. Both  $\nabla \Phi$  &  $\nabla p$  both point inward, so that  $E_r$  and  $\nabla p$  point in opposite directions. Hence, the expression (7.2) is not satisfied before the bias electrode is energized.

There are at least two possible explanations for this disagreement. If temperature gradients had been kept in the model, then additional terms would appear in equation 7.1. There

is no experimental evidence that ion temperature gradients are large in HSX, so this explanation seems unlikely. A second explanation is that there is some externally driven radial current flowing in the plasma before the electrode voltage is applied. A possible source for such a current would be direct loss of high energy electrons driven out of the confinement volume by the ECH. Just as in the bias case, a return current would flow to maintain a neutral plasma, causing the plasma to acquire a positive electric field. A similar effect was observed during perpendicular neutral beam injection in W7-A, where ion on loss orbits were through to drive the electric field strongly negative.<sup>2</sup>

Assume for the moment that the latter explanation is correct: there is some radial current flowing before the electrode bias is applied. Using the relationship between the plasma and floating potentials,  $\Phi_p = V_f + \kappa T_e$ , the electric field term in equation (7.1) can be written as

$$\langle \mathbf{E}_r \cdot \nabla \psi \rangle = - \left( \frac{dV_f}{d\psi} + \kappa \frac{dT_e}{d\psi} \right) \langle \nabla \psi \cdot \nabla \psi \rangle \quad (7.3)$$

To measure the LHS of (7.1), note that at steady state,

$$\langle \mathbf{J} \cdot \nabla \psi \rangle = \frac{I}{A_{\text{surf}}} \langle |\nabla \psi| \rangle. \quad (7.4)$$

It is assumed that the return current is uniformly distributed over the magnetic surface.

With these observations, the version of equation (7.1) before bias is given by

$$\frac{\langle |\nabla \psi| \rangle}{A_{\text{surf}}} I_{\text{pre-bias}} = \sigma_{\perp} \left( \left( \frac{dV_f}{d\psi} \right)_{\text{pre-bias}} + \kappa \frac{dT_e}{d\psi} \right) \langle \nabla \psi \cdot \nabla \psi \rangle + \frac{\langle \nabla p_i \cdot \nabla \psi \rangle}{eN_i}. \quad (7.5)$$

During the bias, the total return current is given by  $I_{\text{total}} = I_{\text{electrode}} + I_{\text{pre-bias}}$ . This leads to the version of equation (7.1) during bias as

$$\frac{\langle |\nabla \psi| \rangle}{A_{\text{surf}}} I_{\text{total}} = \sigma_{\perp} \left( \left( \frac{dV_f}{d\psi} \right)_{\text{during-bias}} + \kappa \frac{dT_e}{d\psi} \right) \langle \nabla \psi \cdot \nabla \psi \rangle + \frac{\langle \nabla p_i \cdot \nabla \psi \rangle}{eN_i} \quad (7.6)$$

where it has been assumed that the electron temperature and ion pressure gradients do not change when the bias is applied. Subtraction (7.5) from (7.6) yields

$$\frac{\langle |\nabla\psi| \rangle}{A_{\text{surf}}} I_{\text{electrode}} = \sigma_{\perp} \left( \left( \frac{dV_f}{d\psi} \Big|_{\text{during-bias}} - \frac{dV_f}{d\psi} \Big|_{\text{pre-bias}} \right) \langle \nabla\psi \cdot \nabla\psi \rangle \right) \quad (7.7)$$

The derivative of the potential with respect to the toroidal flux can be calculated from the floating potential measurements, once the data has been mapped from physical space to flux coordinates. The terms  $\langle \nabla\psi \cdot \nabla\psi \rangle$ ,  $\langle |\nabla\psi| \rangle$ , and the area of the surfaces ( $A_{\text{surf}}$ ) are calculated for many surfaces as part of the Hamada basis vector calculation. Combining these results allows the experimental radial conductivity to be calculated as

$$\sigma_{\perp} = \frac{\langle |\nabla\psi| \rangle}{\langle \nabla\psi \cdot \nabla\psi \rangle A_{\text{surf}}} \frac{I_{\text{electrode}}}{\frac{d}{d\psi} (V_f \Big|_{\text{during-bias}} - V_f \Big|_{\text{pre-bias}})} \quad (7.8)$$

The neoclassical radial conductivity is calculated using equation (6.26). A Monte-Carlo error estimate technique is used to estimate the error in the calculation. The input parameters such as the ion temperature, plasma density, and neutral hydrogen density are repeatedly varied within their estimated uncertainties, and the neoclassical damping rates and radial conductivity are calculated and stored at each iteration. The error in each neoclassical quantity is calculated as the standard deviation of the set of calculations. This process is repeated until the error estimates have stabilized. In the plots to follow, the errors in the modeling will be shown as shaded bands surrounding the most likely values.

These neoclassical calculations require profiles of the plasma density, ion temperature, and neutral atom density. The plasma density profile in these calculations is derived from a combination of Mach probe and the interferometer data. Recall that the fit parameter  $\Gamma_o$  in (2.7) represents the average  $I_{\text{sat}}$  collected by the six tips of the probe. Profiles of this parameter are measured as part of the damping rate profile measurement. An approximate electron temperature

profile is calculated, enabling the  $I_{\text{sat}}$  profile to be converted to a plasma density profile. This density profile is then scaled so that its line average matches the interferometer line average density. As it is difficult to quantify the error in this calculation, it is assumed that there is a 25% error in the local plasma density calculation. The ion temperature is taken to be 15eV at the edge, with a parabolic profile reaching 25eV in the core. These numbers are in keeping with the Doppler spectroscopy measurements presented in Chapter 3. An error of 5eV is used to account for both measurement errors and profile effects. The error bars on the neutral densities are very difficult to determine. For this work, it will be assumed that the atomic hydrogen density is the same in discharges with probes as those without. Asymmetric errors on the neutrals are assumed, with a 100% uncertainty on the upper side (i.e. a neutral density of  $1 \times 10^{10} \text{ cm}^{-3}$  has an uncertainty on the upper side of  $1 \times 10^{10} \text{ cm}^{-3}$ ), and an uncertainty of 30% on the lower side.

As a final note on the neoclassical calculations, it is shown in Appendix 5 that magnetic islands inside the last closed magnetic surface (LCMS) can cause local regions of higher neoclassical viscous damping. In particular, the  $\iota=12/11$  island chain is present in the QHS vacuum configuration, and was shown to cause an increase in the modeled viscous damping on surfaces very near the island chain. In the following presentation, the experimental evidence does not indicate any extra viscous damping in the vicinity of this islands. This could be due to the fact that the spatial resolution of the measurements was not sufficient to resolve the feature. In any case, the Hamada spectrum used in the neoclassical calculations in this chapter will not include the surfaces immediately adjacent to the islands. This area is a subject for future research.

An example of the radial conductivity in the QHS configuration is shown in figure 7.1. This experiment/model comparison forms the basis for other comparisons to follow, and will be studied in some detail. The floating potential profiles both before and during electrode bias are illustrated in the left hand frame. The profiles have been mapped to flux coordinates for this calculation, enabling the potential gradient  $d\Phi/d\psi$  to be calculated. The radial conductivities are compared in the right hand frame. The solid curve at the top represents the measured radial conductivity.

There are three theoretical calculations shown. The curve with a dashed line (2<sup>nd</sup> from top) represents the neoclassical radial conductivity, including all magnetic field ripples and ion-neutral friction. The curve beneath it (dash-dot) illustrates the neoclassical calculations without neutrals; only magnetic field ripples contribute to flow damping in this calculation. The lowest curve (dot-dot) represents the damping due to neutrals only; the viscous frequencies of equation (6.26) were set to zero in calculating this curve. The combination of viscous damping and ion-neutral friction is not sufficient to match the measured radial conductivity.

Recall from Chapter 4 that the floating potential profiles measured on the high and low field sides are nearly identical when mapped to toroidal flux (see Section 4.4). The radial conductivity measurement only depends on measurements of  $d\Phi/d\psi$ . This implies that the experimental radial conductivity would not be different if the high field side (HFS) measurements were used in the calculation instead of measurements taken on the low field side (LFS).

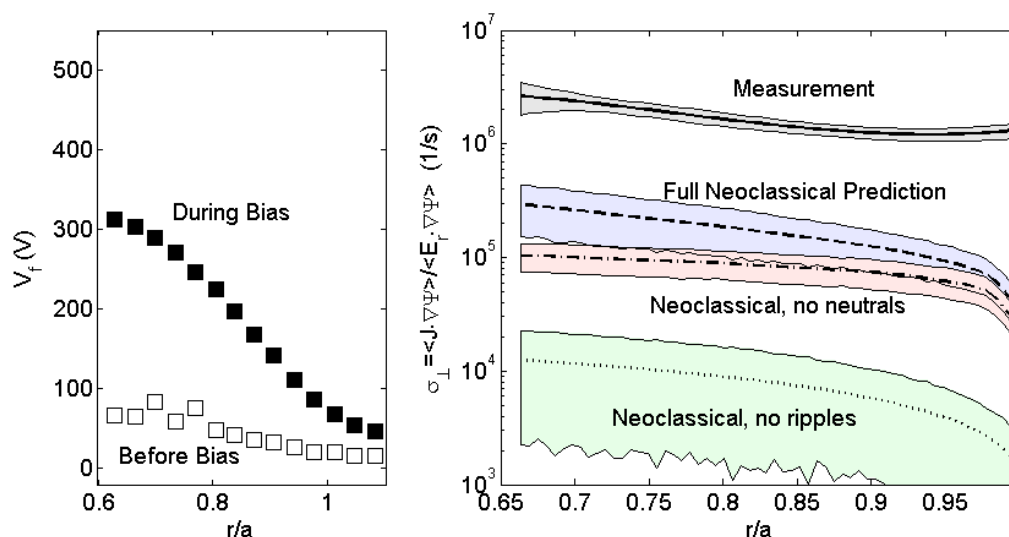


**Figure 7.1: Floating potential profiles before and during electrode bias (left), and a comparison of the measured radial conductivity to the neoclassical predictions (right), for the QHS configuration with a  $n_e=1 \times 10^{12} \text{ cm}^{-3}$  and  $\sim 350 \text{ V}$  electrode bias.**

Even though it is clear that the radial conductivity is not described by neoclassical theory, it is useful to examine the neoclassical calculation in this "base comparison" a little further. Figure

7.2 illustrates the interaction between viscosity and neutrals more clearly. The bottom curve is the same as in the bottom curve on the right of figure 7.1; it is the radial conductivity with all field ripples set to zero. The next curve up in figure 7.2 represents the radial conductivity due to neutrals and the  $(n,m)=(4,1)$  component of the field only. Even in this calculation with perfect quasi-symmetry, the radial conductivity is enhanced compared to the neutrals only case. This has been pointed out in the context of the perfectly axisymmetric tokamak, where the interaction of the  $(n,m)=(0,-1)$  variation in  $|B|$  and neutrals can result in a large enhancement of the radial conductivity compared to the classical value.<sup>3</sup> The third curve in figure 7.2 illustrates the neoclassical radial conductivity including all symmetry breaking terms. Note that the largest increment in radial conductivity comes from adding the main helical spectral component; all of the symmetry breaking terms only increase the radial conductivity by a factor of  $\sim 2$ . The measured radial conductivity is shown as the top curve. The error bars have been removed from the plot for clarity; see figure 7.1 where they are properly included.

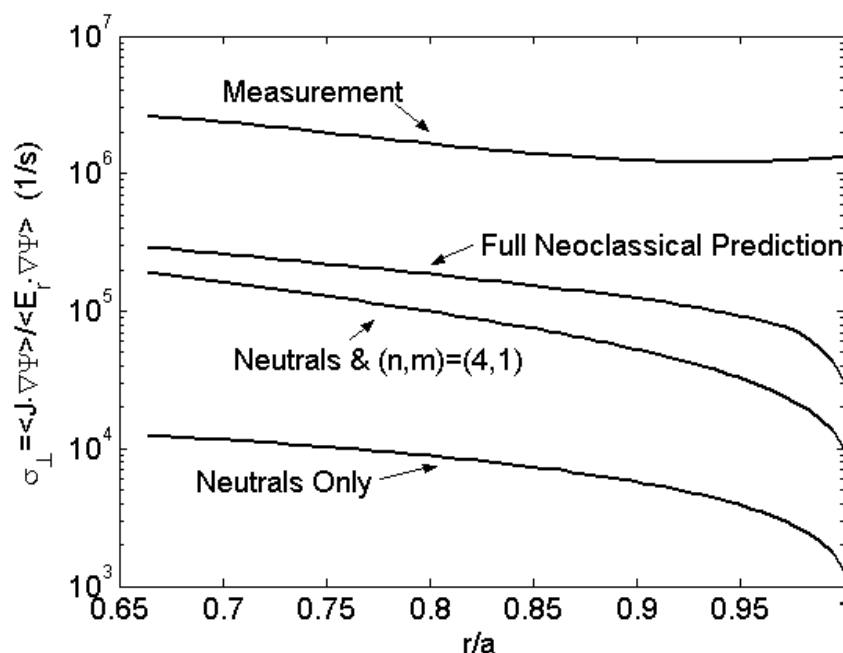


**Figure 7.2: Study of the interaction of neutrals and viscosity in the calculation of the radial conductivity. The most important spectral term in determining the radial conductivity is the  $(n,m)=(4,1)$  main helical component.**

Similar theory/experiment comparisons have been made for other combinations of plasma parameters. An example where the plasma density is the same as above but the electrode voltage is increased to 550V is shown in figure 7.3. The floating potential has gone to a higher values than in figure 7.1, but the radial conductivity is approximately the same. As before, this radial conductivity is anomalously large.

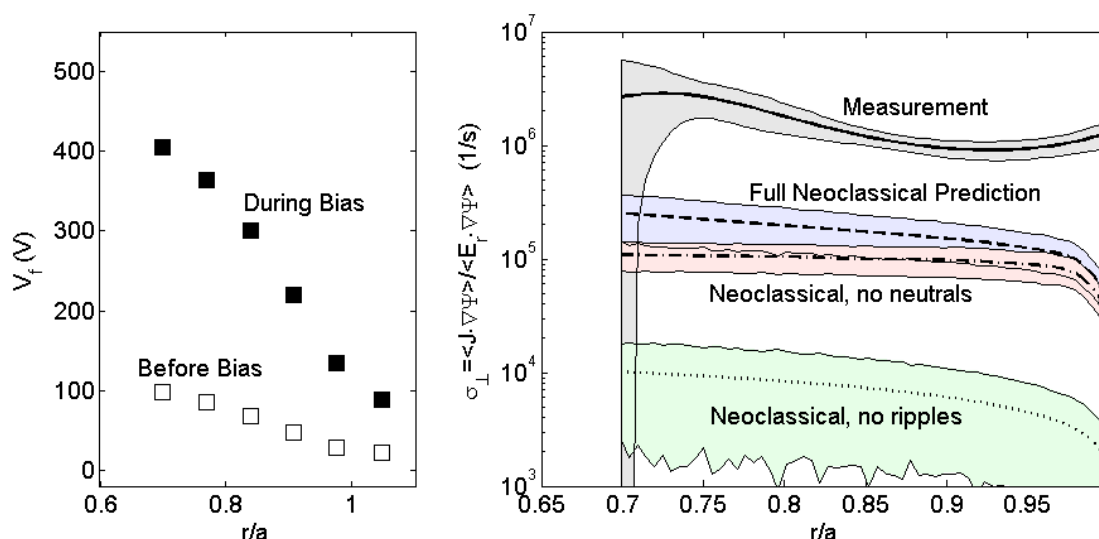


Figure 7.3: Floating potential profiles before and during electrode bias (left), and a comparison of the measured radial conductivity to the neoclassical predictions (right), for the QHS configuration with a  $n_e=1 \times 10^{12} \text{ cm}^{-3}$  and  $\sim 550 \text{ V}$  electrode bias.

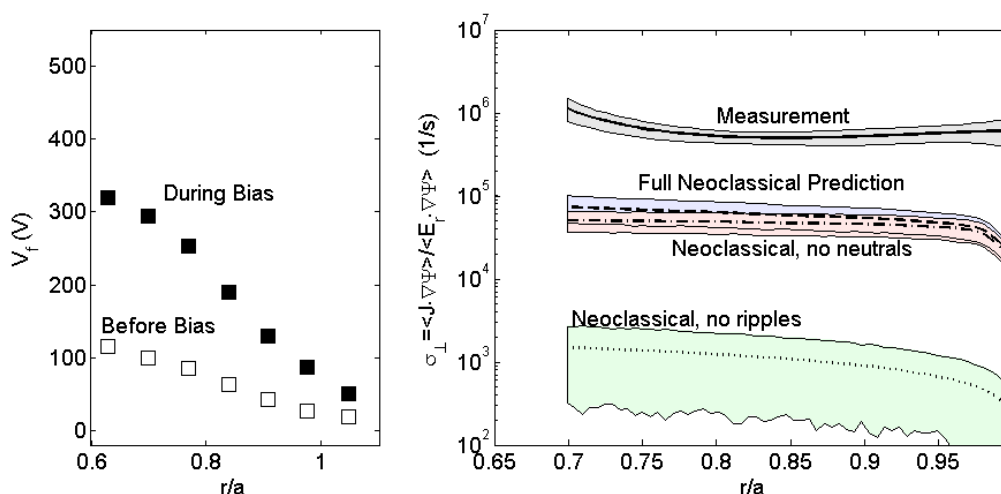
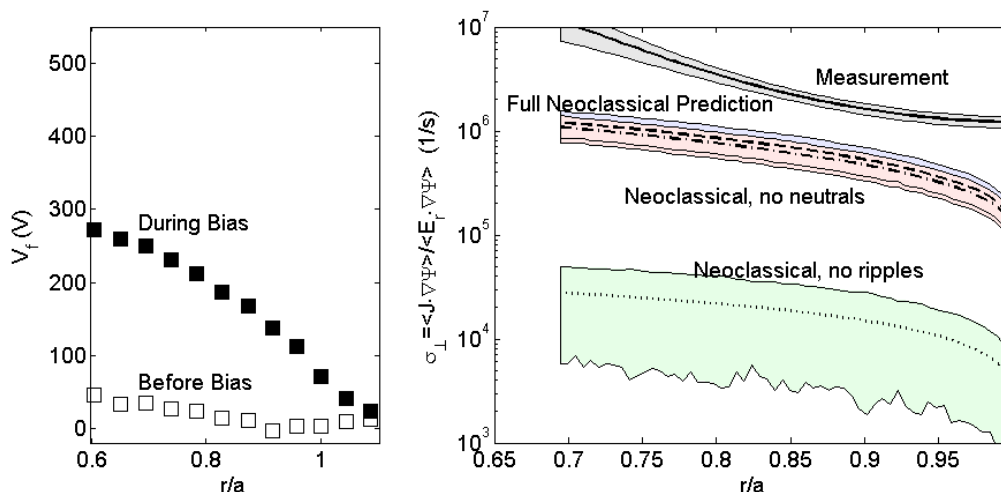


Figure 7.4: Floating potential profiles before and during electrode bias (left), and a comparison of the measured radial conductivity to the neoclassical predictions (right), for the QHS configuration with a  $n_e=5 \times 10^{11} \text{ cm}^{-3}$  and  $\sim 350 \text{ V}$  electrode bias.

As a third comparison for the QHS configuration, the measured and modeled radial conductivity for a line average density of  $5 \times 10^{11} \text{ cm}^{-3}$  are illustrated in figure 7.4. The measured radial conductivity is lower in this case than the previous cases, mainly due to the decreased electrode current at lower plasma density. The neoclassical prediction is also substantially lower, and the net result is that the radial conductivity continues to be anomalous.

These types of measurements have also been made in the Mirror configuration of HSX, and an example is shown in figure 7.5. The agreement between the measured and modeled radial conductivity is better in this case, principally due to an increase in the prediction of the modeling. The neutrals contribute an insignificant amount to the modeling, due to the large increase in neoclassical viscous damping in this configuration. Interestingly, in a comparison between this 10% Mirror data and the 16% Mirror neoclassical calculation, the magnitudes of the theory and experiment are quite comparable. As a general note, the data in this chapter will show better neoclassical theory/experiment agreement for the Mirror configuration than the QHS.



**Figure 7.5: Floating potential profiles before and during electrode bias (left), and a comparison of the measured radial conductivity to the neoclassical predictions (right), for the Mirror configuration with a  $n_e = 1 \times 10^{12} \text{ cm}^{-3}$  and  $\sim 350 \text{ V}$  electrode bias.**

Given that the radial conductivity appears to be anomalous, the radial conductivity from the model by Rozhansky and Tendler<sup>1</sup> has been compared to the data. This model was derived

for the case of a biased electrode in circular tokamak geometry. In their derivation, anomalous transport was assumed to be present, giving rise to sufficient damping of toroidal flows to balance the  $\mathbf{J}_r \times \mathbf{B}_p$  torque. Under the assumption that the radial gradients in the poloidal flow are sufficiently small, the radial conductivity is given by:

$$\sigma_{\perp} = -\frac{c^2 m_i N_i q \sqrt{\pi} v_{ti}}{2R_o B_o^2}. \quad (7.9)$$

This expression does a reasonable job of predicting the radial conductivity of the TUMAN-3 tokamak in the L-mode regime (low electrode voltage and high electrode current).<sup>4</sup>

This same expression can be derived from the neoclassical treatment in Chapter 6.<sup>5</sup> Simply assume the Fourier spectrum of a rippled tokamak with N toroidal field coils,

$$\mathbf{B} = B_o (1 - \epsilon_T \cos(\alpha) + \epsilon_R \cos(N\zeta)), \quad (7.10)$$

and use the large aspect ratio tokamak basis vectors,<sup>6</sup> while neglecting the contribution of any neutrals. These approximations can be used to calculate the viscous frequencies  $\nu_{\alpha}$ ,  $\nu_{\zeta}$ ,  $\nu_{\alpha}^{(P)}$ , and  $\nu_{\zeta}^{(P)}$  in (6.18). When these expressions are inserted into the formula (6.26), the radial conductivity becomes:

$$\sigma_{\perp} = -\frac{c^2 m_i N_i q \sqrt{\pi} v_{ti} N \epsilon_R^2}{2R_o B_o^2 (\epsilon_T^2 + N \epsilon_R^2)}. \quad (7.11)$$

Taking the limit that  $N \epsilon_R^2 \gg \epsilon_T^2$  yields the result presented in (7.9).

A comparison between this radial conductivity and the QHS data is shown in figure 7.6, for the QHS case with 350 V of electrode voltage at a line average density of  $1 \times 10^{12} \text{ cm}^{-3}$ . This somewhat heuristic expression fits the HSX data more closely than the neoclassical modeling presented in the previous sections. This result illustrates that the radial conductivity in HSX is not so dissimilar to that in an axisymmetric device. The large divergence between the model and measurement at the very edge is due to the density scaling in the Rozhansky and Tendler expression.

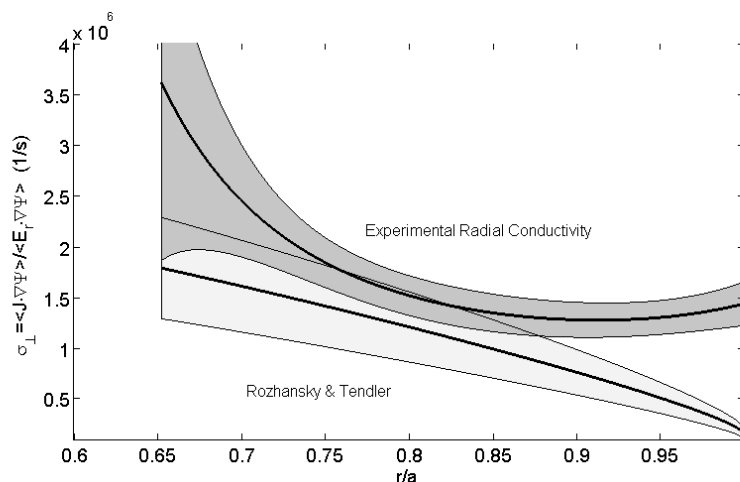


**Figure 7.6: Comparison between the experimental radial conductivity (dark region) and the model of Rozhansky and Tendler (light region).**

As a final note for this section, the measured values for the radial conductivity can be compared to the radial conductivity derived by Okabayashi and Yoshikawa.<sup>7</sup> Their Pfirsch-Schlueter regime expression has been modified to include toroidicity by Coronado and Talmadge.<sup>8</sup> The result is

$$\sigma_r = \frac{c^2 m_i N_i}{B^2} v_{in} (1 + 2q^2) \quad (7.12)$$

Inserting HSX values for this expression leads to a prediction of  $\sigma_r \sim 4 \times 10^4 \text{ s}^{-1}$ . As expected, this value is substantially smaller than the experimental value.

### 7.1.2: Radial Conductivity Scaling With Density

The density scaling of the plasma conductivity has also been studied in the QHS configuration. A critical point in the interpretation of these experiments is the similarity of the plasma parameter profiles at different densities, since detailed profiles of the floating potential and plasma density were not necessarily measured at each of the plasma densities in this series of experiments. To clarify this point, the LFS Mach probe was held fixed at  $r/a \approx 0.8$  and the large

electrode was held at fixed  $r/a \approx 0.65$ , as the density was scanned by adjusting the external gas fueling. The capacitor bank voltage was held constant in these experiments, but because of the series resistance of the power supply and the increasing electrode current with increasing plasma density, the actual voltage at the electrode decreased slightly as the density was increased. This effect is shown in the left frame of figure 7.7. The figure also illustrates the voltage on the proud pin of the fixed Mach probe both before and during the electrode voltage pulse. The floating potential before the bias pulse decreases as the density increases. The floating potential during the pulse, being determined by the electrode, is constant as a function of density. From this data, it can be inferred that there are not large changes in the electric field profile as the density is scanned.

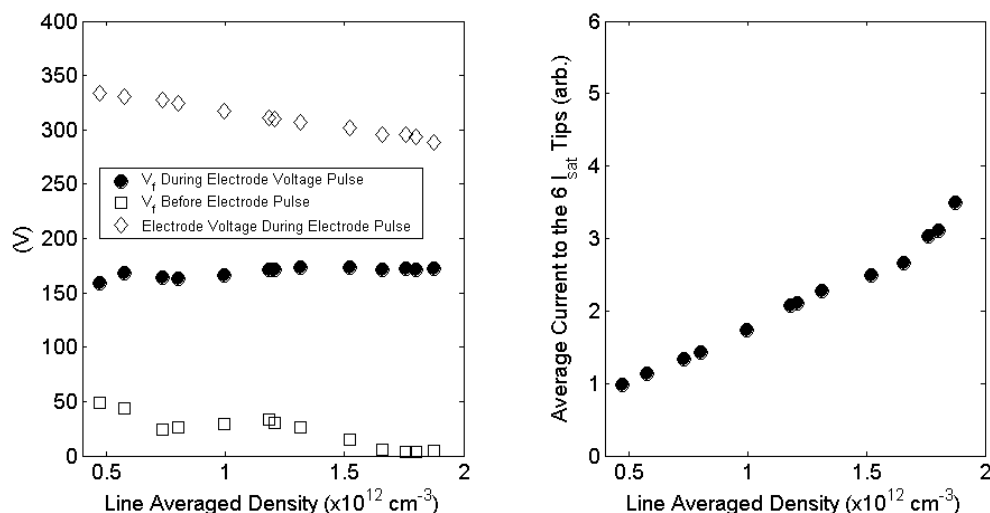


**Figure 7.7: Variation of the floating potential and electrode potential (left) and local  $I_{\text{sat}}$  (right) with line average density.**

It is also observed that the density profile shape is reasonably constant during these experiments. The average  $I_{\text{sat}}$  drawn by the six tips of the Mach probe is shown in the right frame of figure 7.7 as a function of the line average density. The local density at the probe location appears to be related to the line average density in a linear fashion. This implies that to lowest order, the plasma density profile is simply being scaled as the line average density is scanned.

Using the observations from the previous paragraph, we can compare the electrode voltage-electrode current relationship as follows. The radial current density is related to the potential gradient as

$$\frac{d\Phi}{d\psi} = \frac{I_{\text{electrode}}}{\sigma_{\perp} A_{\text{surf}}} \frac{\langle |\nabla\psi| \rangle}{\langle \nabla\psi \cdot \nabla\psi \rangle}. \quad (7.13)$$

Any model for the radial conductivity can be used when evaluating this expression. Integrating this expression from the edge (where the potential is  $\Phi_a$ ) to the surface with the electrode yields

$$\Phi(\psi_{\text{electrode}}) = \Phi_a + \int_{\psi_a}^{\psi_{\text{electrode}}} \frac{I_{\text{electrode}}}{\sigma_{\perp} A_{\text{surf}}} \frac{\langle |\nabla\psi| \rangle}{\langle \nabla\psi \cdot \nabla\psi \rangle} d\psi. \quad (7.14)$$

Hence, an effective impedance can be defined as

$$R_{\text{eff}} = \int_{\psi_a}^{\psi_{\text{electrode}}} \frac{1}{\sigma_{\perp} A_{\text{surf}}} \frac{\langle |\nabla\psi| \rangle}{\langle \nabla\psi \cdot \nabla\psi \rangle} d\psi. \quad (7.15)$$

This quantity can be compared to the measured resistance, defined as

$$R_{\text{measured}} = \frac{V_{\text{plasma}}}{I_{\text{electrode}}}. \quad (7.16)$$

$V_{\text{plasma}}$  is the voltage which is dropped across the plasma, with the following caveats. Not all of the electrode voltage is dropped across the plasma. Typically, the separatrix is at approximately 20-50 Volts during the bias pulse, as illustrated in the floating potential profiles above. There is also some sheath drop at the electrode, so that the measured electrode voltage is not the plasma potential on the surface where the electrode resides. This sheath drop is difficult to measure, and will assumed for purposes of this calculation to be 50 V as well, equal to the approximate edge electron temperature as measured by swept probes in comparable plasmas. In summary, it is assumed that the voltage dropped across the plasma is equal to the electrode voltage minus 100V.

In the calculations of the neoclassical radial conductivity and damping rates for the density scan, a parabolic density profile and a flat ion temperature profile were assumed. The value of the ion temperature was selected to vary weakly with density as shown in Chapter 4. The atomic hydrogen was assumed to have a flat profile, and to scale weakly with density, as inferred from DEGAS calculations.<sup>9</sup> The profiles are shown in figure 7.8, with the arrows indicating the progression among the various quantities. These profiles were used to calculate the profile of  $\sigma_{\perp}$ , which was then used in (7.15) to predict the resistance seen by the electrode.

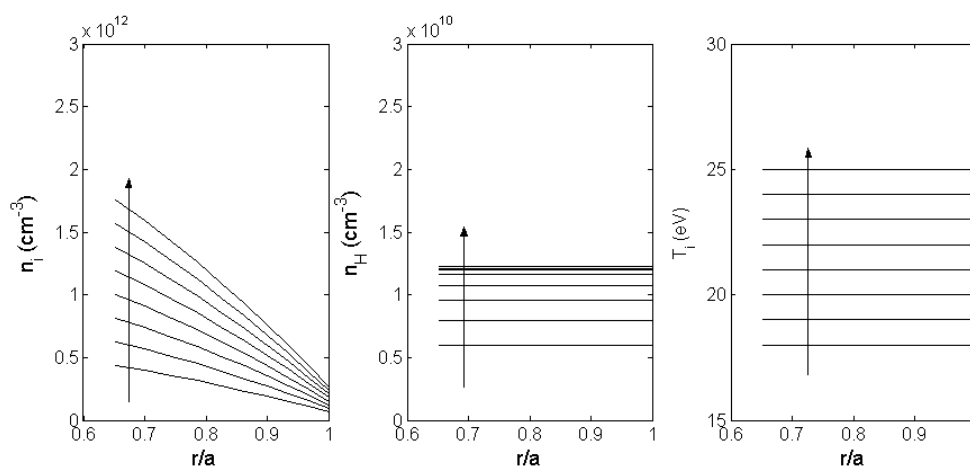


**Figure 7.8: Scaling of the profiles of ion density, atomic hydrogen density, and ion temperature used in the neoclassical modeling.**

The scaling of the electrode resistance with the line average density for the QHS configuration is shown in figure 7.9. This analysis was performed by analyzing the steady state voltage and current of the electrode for each bias pulse independently. With 6 biased electrode pulses per discharge and approximately 70 discharges in this data set, there are approximately 420 data points on these graphs. The resistance seen by the electrode scales with density like  $1/n_e^{1.5}$ . This scaling should be taken with some caution, as the resistance probably depends on the ion temperature and other factors that are also changing as the plasma density changes. Changes in the sheath and separatrix potentials may also impact the observed scaling.

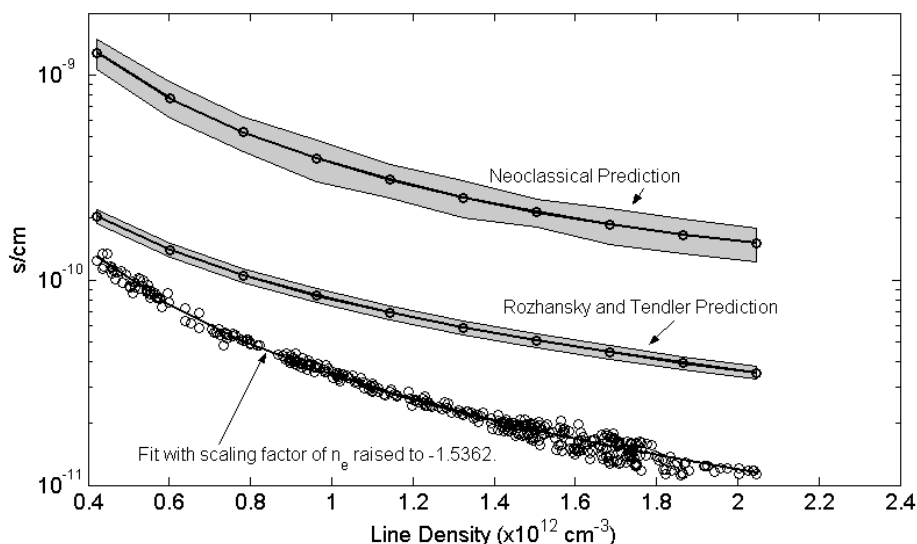


**Figure 7.9: Scaling with line average density of the resistance seen by the electrode in the QHS configuration. See text for descriptions of the models.**

Figure 7.9 also displays the predictions based on the two models under consideration in this chapter. While both the models and the data have a similar scaling with density, there is a large discrepancy between the data and the neoclassical prediction. As seen in the detailed profile data of Section 7.2.1, the neoclassical modeling indicates that the plasma should be less conductive, or more resistive, than indicated by the data. The Rozhansky and Tendler expression appears to fit the data more closely than the neoclassical modeling.

A similar scaling experiment has been performed in the Mirror configuration, as displayed in figure 7.10. These discharges were part of a series of discharges measuring the radial conductivity profiles at densities of  $5 \times 10^{11}$  and  $1 \times 10^{12} \text{ cm}^{-3}$ , and the shot to shot variation in the data provides the density scaling shown here. The scaling with density appears to be  $R \propto n_e^{-1.4}$ , a scaling which is quite similar to the QHS scaling. The caveats noted above in regard to this scaling apply here as well. The modeling agrees much more closely with the measurements in these discharges, compared to the QHS comparison.

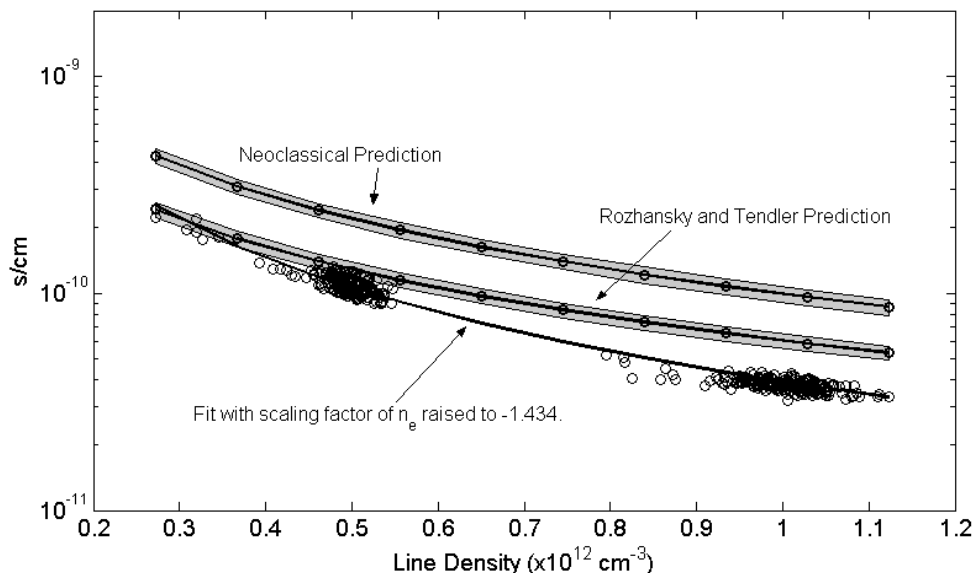


**Figure 7.10: Scaling with line average density of the resistance seen by the electrode in the Mirror configuration. See text for descriptions of the models.**

### 7.1.3: Comparison Between the Measured and Modeled Steady State Plasma Flow Directions.

Continuing in the steady state comparison, the next subject is a comparison of the measured and predicted steady state direction of the plasma flows.

The neoclassical prediction for the steady state plasma flow was specified in Chapter 6 as, for instance,

$$\mathbf{U}(t) = (V_1 \mathbf{e}_\alpha + B^\zeta G_1 \mathbf{e}_\zeta) + (V_2 \mathbf{e}_\alpha + B^\zeta G_2 \mathbf{e}_\zeta), \quad (7.15)$$

where the quantities  $V_1$ ,  $V_2$ ,  $G_1$ , and  $G_2$  were specified in that chapter. To compare this formula to the measurements, it is necessary to know the Hamada basis vectors  $\mathbf{e}_\alpha$  and  $\mathbf{e}_\zeta$ . This is an example of a situation where the knowledge of the specific HSX Hamada basis vectors is very important. Using the tokamak basis vectors for HSX would make no sense in this context, given the strong shaping of the plasma column and the helical magnetic axis.

The steady state flow direction can be calculated either directly from the data or from the fits presented in Chapter 4. For instance, the steady state flow can be calculated as

$$\mathbf{U}_{SS} = (C_f \cos(\alpha_f) + C_s \cos(\alpha_s))\mathbf{b} + (C_f \sin(\alpha_f) + C_s \sin(\alpha_s))\mathbf{n}, \quad (7.16)$$

based on the fits in equation 4.3. In this expression,  $\mathbf{b}$  and  $\mathbf{n}$  are unit vectors parallel to the magnetic field and perpendicular to the field but in the magnetic surface.  $C_f$  is the amount of flow in the fast direction and  $C_s$  is the amount of flow in the slow direction. The angle associated with the fast rising flow is  $\alpha_f$  and with the slow rising flow is  $\alpha_s$ , where the angles are in the  $\mathbf{b}, \mathbf{n}$  plane. Using this definition accounts for the flow due to the biased electrode only; the flow before the electrode was fired has been subtracted off in this formulation.

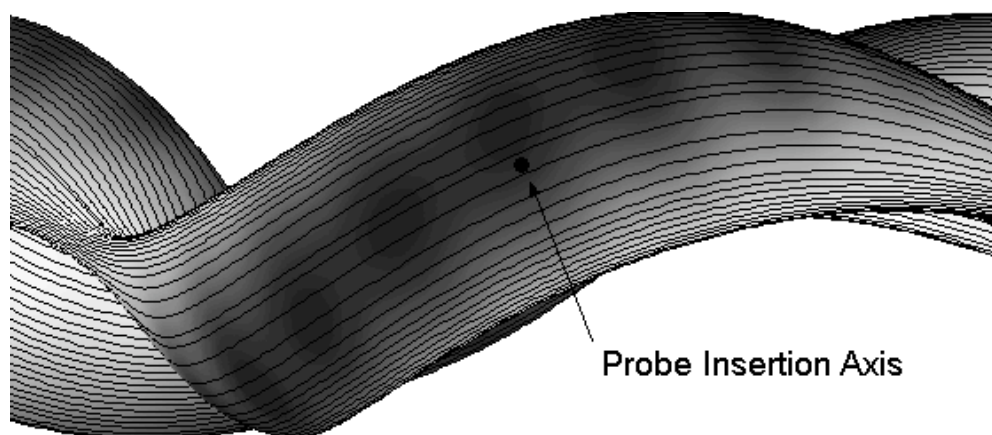


**Figure 7.11: View of the  $|B|$  contours at the location of the low field side Mach probe, as well as the trajectories of magnetic field lines. Dark colors represent regions of lower  $|B|$ .**

Throughout this chapter (and already in figure 4.41), the flow directions are illustrated in polar plots. These polar plots are arranged so that the magnetic field points directly to the right. Figures 7.11 and 7.12 illustrate the contours of  $|B|$  and the trajectories of magnetic field lines, for the low and high field Mach probe insertion locations respectively. The  $|B|$  contours are those of the QHS configuration. Note that the contours of constant  $|B|$  (neglecting symmetry breaking ripples) are more tightly wrapped around the torus than the magnetic field lines. The constant  $|B|$  contours wrap poloidally around the machine once in each of the four field periods, while the  $\ell=1$  magnetic field line wraps poloidally around the machine once per toroidal transit. For all data

in this dissertation, the magnetic field was configured to point in the counterclockwise direction as viewed from the top of HSX. This implies that the "toroidal" magnetic field points toward the right as one faces HSX from the outboard side. The symmetry direction is thus rotated in the counterclockwise direction compared to the magnetic field line.

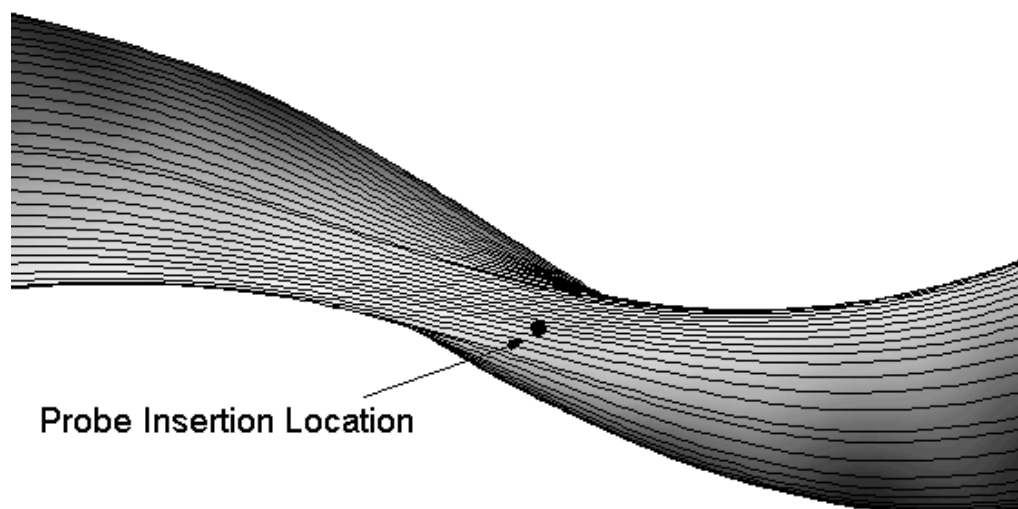


**Figure 7.12: View of the  $|B|$  contours at the location of the high field side Mach probe, as well as the trajectories of magnetic field lines. Dark colors represent regions of lower  $|B|$ .**

A representative example of the theory/experiment flow direction comparison is made in figure 7.13 for the QHS configuration. The Mach probe is at a normalized radius  $r/a \approx 0.9$  with the biased electrode at  $r/a \approx 0.65$ , and the line average density is  $1 \times 10^{12} \text{ cm}^{-3}$ . As discussed before, the magnetic field is aligned to be at zero degrees. The symmetry direction and neoclassically predicted flow direction are shown in the plot, as well as the measured steady state flow direction. The neutral atomic density, line average plasma density for the shot, estimated plasma density at the Mach probe, and the probe location are written on the figure. The estimated uncertainty due to probe misalignment is shown as a gray triangle around the steady state flow direction. All arrows have been normalized to length one, and only the directions should be compared in this figure.

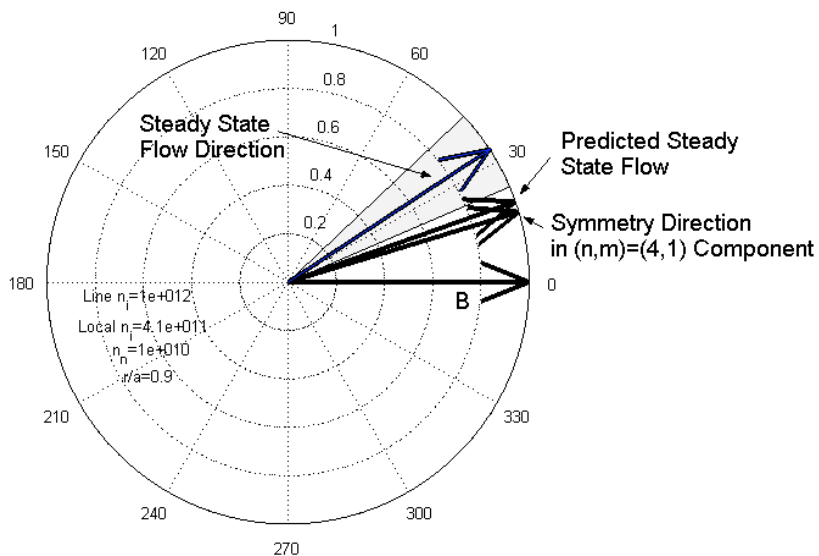


**Figure 7.13: Comparison between the measured plasma flow direction and the neoclassical prediction, for a medium density discharge (line density of  $1 \times 10^{12} \text{ cm}^{-3}$ ). The direction of symmetry in the  $(n,m)=(4,1)$  spectral component and the direction of the magnetic field are also shown.**

It appears that the steady state flow is rotated counter-clockwise with respect to the neoclassical prediction. The predicted steady state flow direction is just barely outside the error bars. The flow angle has a weak variation with density, as is seen in figure 7.14. As the density increases, the direction of the flow induced by the bias is rotated somewhat counterclockwise. The magnetic field is at  $0^\circ$  in this figure. The neoclassical predicted flow direction is essentially unchanged as a function of density at 0.3 radians counterclockwise of the magnetic field.

The steady state flow on the high field side is illustrated in figure 7.15; the flow direction looks similar to that on the low field side from in figure 7.13. The magnetic field is aligned to point directly to the right, and the direction of symmetry is slightly counterclockwise of the magnetic field. The neoclassically predicted steady state flow is somewhat counterclockwise of the symmetry direction. The steady state bias induced flow direction is counterclockwise of all these directions, just as on the low field side.

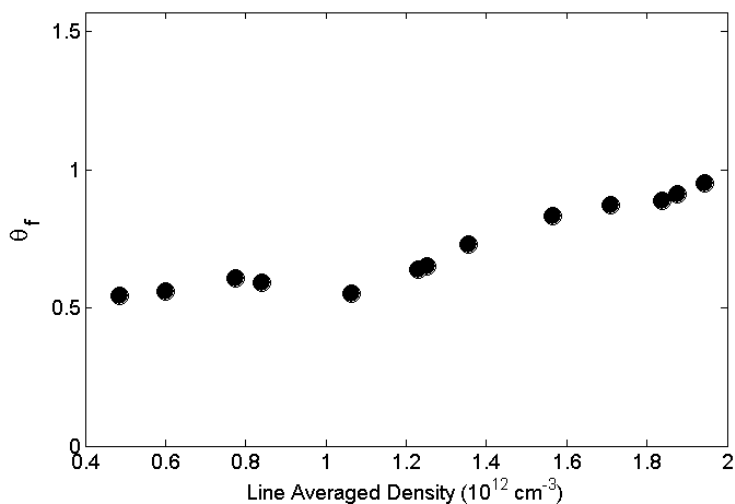


**Figure 7.14: The variation of the measured flow angle with line average density in the QHS configuration on the LFS, at  $r/a=0.9$ .**

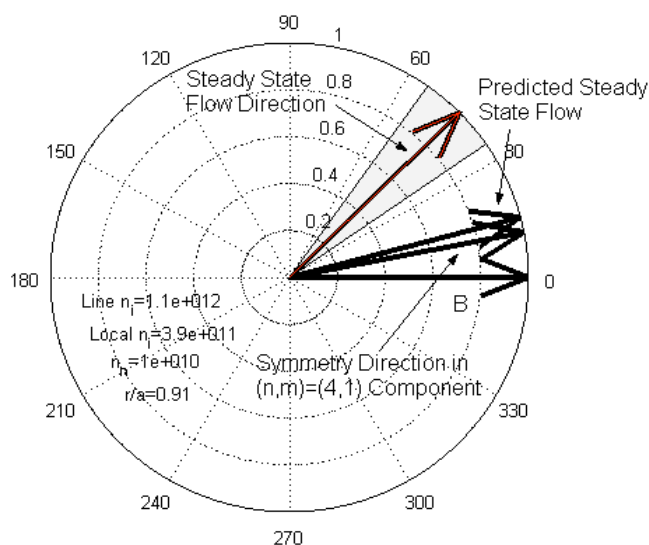


**Figure 7.15: Predicted and measured flow directions on the HFS in the QHS configuration.**

The same comparison of predicted and measured steady state flow direction is shown for the Mirror configuration on the low field side in figure 7.16. Compared to the similar QHS measurements in figure 7.13, the flow is rotated farther away from the direction of symmetry in the  $(n,m)=(4,1)$  spectral component. This is in keeping with expectations, and has been observed already in figure 4.41.

On the other hand, the neoclassical prediction is not so different between the QHS and Mirror configurations. There is a large separation between the neoclassical fast and slow time scales, even in the Mirror configuration. As long as the slow time scale does not begin to approach the fast time scale, the predicted direction of flow does not change appreciably. This is why the QHS slower neoclassical damping rate can be much slower than the Mirror slow damping rate, yet the direction of neoclassical predicted flow does not change significantly.

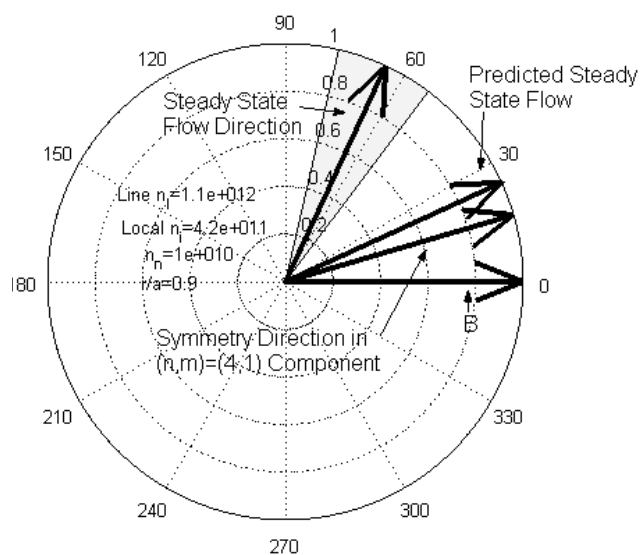


**Figure 7.16: Comparison between the measured plasma flow direction and neoclassical prediction for the Mirror configuration on the low field side.**

#### 7.1.4: Comparison Between Hydrogen and Deuterium QHS Discharges.

In addition to comparisons between the different configurations of HSX, QHS discharges have been made with both hydrogen and deuterium as the working gas. In the comparisons that follow in this section, data from a single day is presented where the working gas was switched from hydrogen to deuterium in the middle of the day. The goal of these experiments was to determine if the mass scaling in the modeling bears out in the data. The radial conductivity parameters will be examined in this section as a test of the mass scaling.

The floating potential profiles in the hydrogen and deuterium cases are shown in figure 7.17. The profiles are quite similar, once more indicating that these smooth potential profiles are ubiquitous features of biased discharges in HSX. On the other hand, the current drawn by the electrode was different in the two cases, which will lead to a difference in the radial conductivity.

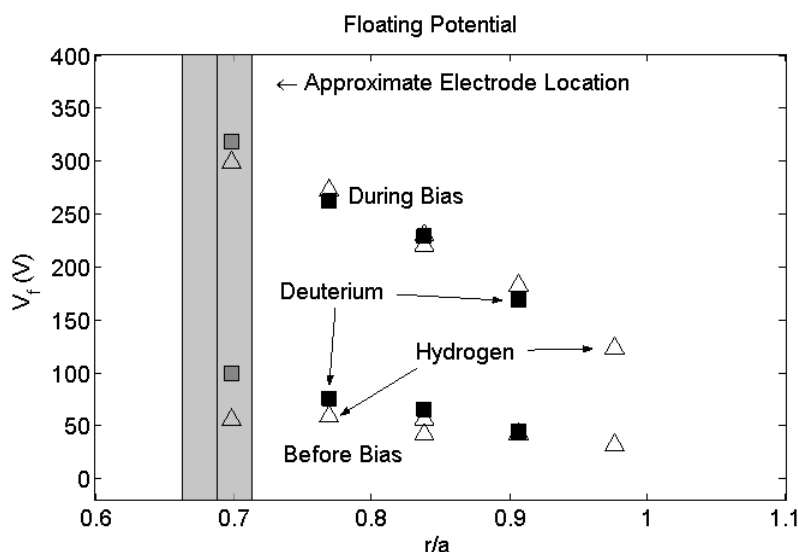


**Figure 7.17: Comparison of the floating potential profiles for deuterium (solid squares) and hydrogen (open diamonds) discharges.**

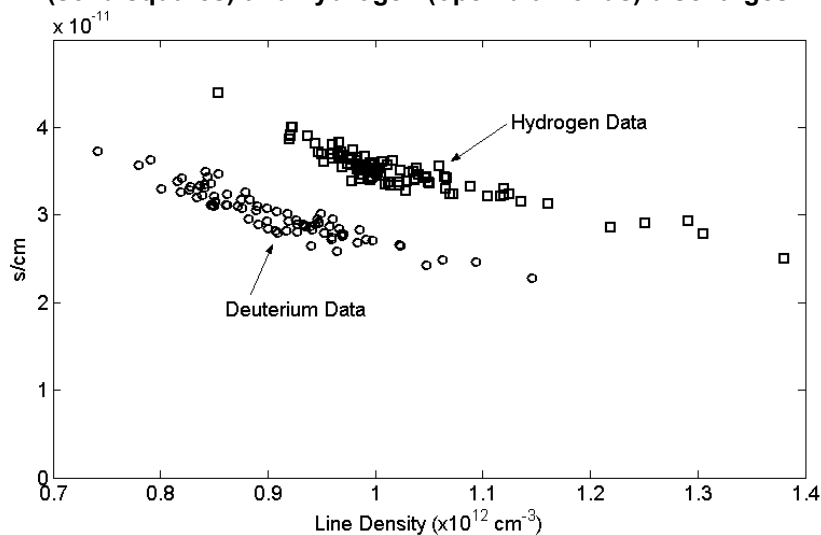


**Figure 7.18: The density scaling of the electrode resistance in deuterium and hydrogen.**

The scaling of the resistance seen by the electrode for the two gases is illustrated in figure 7.18. The Mach probes were moved around during these discharges while the operator

was attempting to maintain a constant density. The shot to shot variation in the density leads to the scaling data presented in the figure. The analysis was performed by analyzing the steady state electrode voltage and current for each bias pulse independently. With three biased electrode pulses per discharge and ~25 discharges for each gas, there are ~75 data points on these graphs.

This data provides a unique opportunity to test the modeling. As discussed in detail in Chapter 3, the neutral density in these discharges has been diagnosed through a combination of  $H_{\alpha}$  measurements and the DEGAS<sup>10</sup> code. The neutral density determined this way is approximately consistent with the ion temperature measured using Doppler spectroscopy. Further, the particle diffusion coefficient deduced from this data agrees well with that determined from perturbative particle transport experiments.<sup>11</sup>

Even with this evidence that the inferred neutral density is approximately correct, it is interesting to ask what neutral density is required so that the measured and modeled radial conductivities are in agreement. Figure 7.19 illustrates the deuterium and hydrogen data, along with the neoclassical predictions as calculated from equation (7.15). The neutral density in these calculations was increased so that the modeling and measurements for deuterium agreed. This required a factor of ~40 increase in the neutral deuterium density compared to the estimate of  $n_n \sim 7 \times 10^9 \text{ cm}^{-3}$ . This same neutral density was then used in calculating the predicted resistance for hydrogen. Using the same neutral density in hydrogen and deuterium is justified because the  $H_{\alpha}$  signals were virtually identical for the two cases (both  $H_{\alpha}$  and  $D_{\alpha}$  are in the pass band of the detectors).

The result in figure 7.19 illustrates that the measured mass scaling of the radial conductivities is not as predicted. The predicted ratio of conductivities is  $\approx 1.7$  for this case with artificially large neutrals, but the measured ratio is 1.3. Hence, we have further reason to believe that some non-neoclassical effect is enhancing the radial conductivity, not simply a severe underestimation of the neutral density.

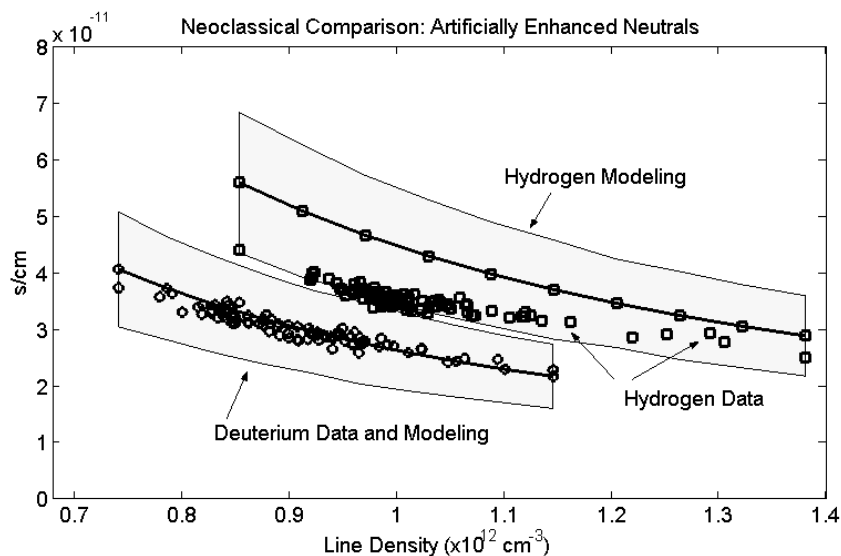


**Figure 7.19: The density and mass scaling of the electrode resistance, compared to a neoclassical calculation. The neutral density was been artificially increased so that the deuterium measurement and modeling agree.**

Note that according to the model by Rozhansky and Tendler, the radial conductivity should scale as  $m_i^{1/2}$ . For these experiments, this ratio of the resistances is predicted to be  $2^{1/2}=1.414$ . This is significantly closer to the scaling observed in the experiment.

### 7.1.5 Summary

This section has compared the steady state biased plasma conditions to various models, including the neoclassical modeling developed in this thesis and the model developed by Rozhansky and Tendler. The major conclusion of this section is that the radial conductivity in HSX is anomalously large. This has been verified in detail for the QHS configuration, where the radial conductivity has been studied as a function of minor radius for different electrode voltages, plasma densities, and working gasses. In all of these cases, the measured radial conductivity is  $\sim 10$  larger than the neoclassical prediction. On the other hand, the data has been compared with the expression for the radial conductivity in a tokamak with anomalous viscosity developed by Rozhansky and Tendler. This expression shows agreement with the QHS data to within a factor of 2-3.

The radial conductivity in the Mirror configuration of HSX has also been compared to the neoclassical predictions. The measurements in this case agree to within a factor of 2-3 with the neoclassical prediction. The measurements are generally within a factor of 2 of the Rozhansky and Tendler prediction.

Finally, experiments comparing hydrogen and deuterium plasmas showed that the radial conductivity is a factor of  $\sim 1.3$  lower with deuterium. This is in approximate agreement with the mass<sup>1/2</sup> scaling of the Rozhansky and Tendler model.

## 7.2: Comparison between the Plasma Flow and Floating Potential Rise Measurements and Neoclassical Modeling

The modeling presented in Chapter 6 makes a number of predictions about the flow spin-up and electric field formation. In summary form, the “Forced  $E_r$ ” model developed during this research assumes or predicts that:

- #1: The electric field changes very quickly, essentially on the electrode voltage time scale.
- #2: One component of the plasma flow will rise on the same time scale.
- #3: There will be a large initial spike in the electrode current when the voltage is first applied.
- #4: A second component of the plasma flow will rise with a time scale  $1/v_F$ , as defined in (6.90).
- #5: The direction associated with the slow rise will be the parallel direction.
- #6: The direction associated with the fast rise will be the covariant poloidal direction.

Prediction #1 is satisfied by the data. The floating potential is observed to evolve very quickly ( $\sim 1-3 \mu\text{s}$ ) across the entire profile, implying that the electric field grows on that time scale as well. It was this observation of the fast electric field formation that motivated the modeling in the first place.

Prediction #2 is more difficult to verify. There is definitely a component of the flow which rises very quickly, but the time scale is too fast to measure accurately with the Mach probe

diagnostic. Hence, we can say that the observations are at least not inconsistent with the modeling.

Prediction #3 is approximately reproduced in the data. Considering figure 4.23, there is an initial spike of  $\approx 20\text{A}$  in the electrode current before it settles to its steady value during the bias pulse. On the other hand, the spike is smaller than predicted by the model. One possible reason for this discrepancy is that the model is formulated for one flux surface at a time, while the physical electrode current contains information about all surfaces at a larger minor radius than where it resides. The fast, yet finite, time required for the propagation of the electric field information is not included in the model, and may serve to limit the electrode current in real life.

These observations leave predictions 4, 5, & 6 yet to be considered. Making detailed comparisons of these observations is the purpose of the following subsections. Note that the measured time scales are always plotted as the inverse rise or decay time. For instance, the inverse slow flow rise time is simply  $1/\tau_s$ , with  $\tau_s$  defined in equation (4.3), and the inverse fast decay times is  $1/\tau_F$ , as defined in equation (4.5).

## 7.2.1 Radial Profiles of the Flow Rise Parameters

The slow time scale for the flow rise is predicted to occur with an inverse time constant of  $v_F$ , as indicated in prediction #4 above. A comparison between the data and the measured time scales is provided for the QHS configuration in figure 7.20. The profiles are compiled on a shot to shot basis; all data presented in this section is for discharges with a line average density of  $1 \times 10^{12} \text{ cm}^{-3}$  and an electrode voltage of  $\approx 350\text{V}$ . The error bars on the data are representative of the shot to shot reproducibility, while the error band on the neoclassical prediction is derived using the Monte Carlo technique described in Section 7.1. The figure shows data from the high and low field side probes plotted on the same axis; the measurements at these two locations agree well with each other. The numerical values are in agreement with the modeling, both in magnitude and radial profile shape. Given the simplicity of the modeling, the agreement is remarkable.

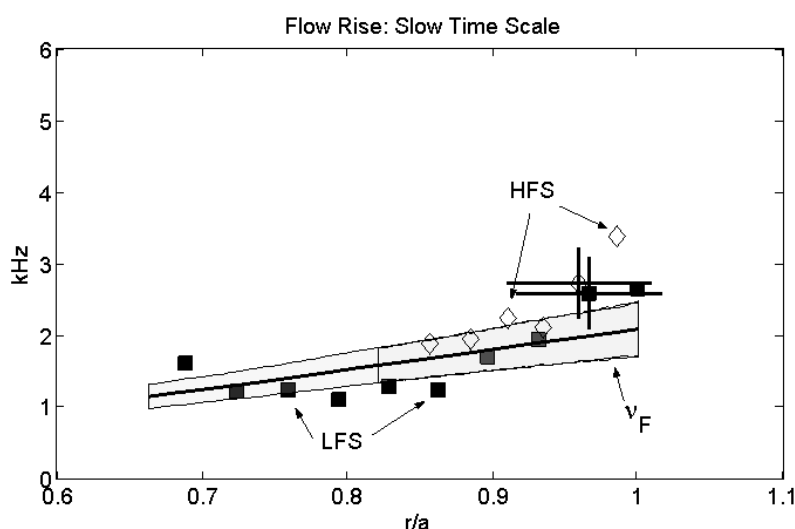


**Figure 7.20: Profile comparison of the measured inverse time scale for the slow flow rise to the modeled frequency  $\nu_F$ , for the QHS case. The different symbols represent measurements made with the LFS (solid squares) and HFS (open diamonds) probes.**

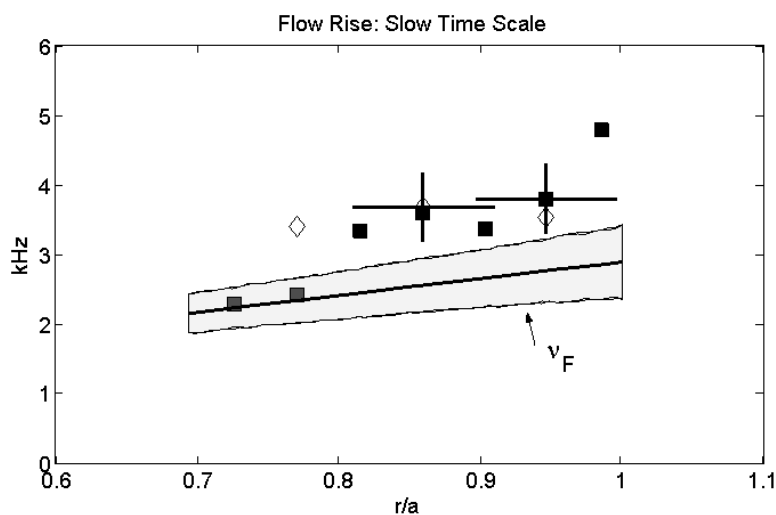


**Figure 7.21: Profile comparison of the measured inverse time scale for the slow flow rise to the modeled frequency  $\nu_F$ , for the Mirror case. Open and closed symbols represent two separate run days with otherwise identical plasma conditions.**

Similar comparisons have been made for Mirror configuration. Figure 7.21 shows the comparison between the measured inverse time scale for the slow flow rise and  $\nu_F$ . The data is taken using the low field side probe, with open and closed symbols representing data taken on

two different days with otherwise identical plasma conditions. The agreement between the model and the data in this case is reasonably good, although the model appears to underestimate the damping.

A very important point is made by this data. The difference in time scales in the modeling is due to neoclassical viscosity. Given that the data do indeed fit the model, this supports the idea that the difference between QHS and Mirror configurations in the data is due to the reduction of neoclassical viscous damping with quasi-symmetry.

## 7.2.2 Density Scaling of the Flow Rise Parameters

The fast floating potential rise at electrode turn-on is a ubiquitous feature of these experiments, and is present at all densities and in all configurations. Hence, the question of interest is the scaling of the inverse rise time of the slow flow with the line average density. This is shown in figure 7.22 for the QHS configuration, where the measurements with the LFS Mach probe have been compared to the modeled rate  $v_F$ . The biased electrode was fixed at  $r/a \sim 0.65$  and the Mach probe at  $r/a \sim 0.9$ . Apart from two points at the lowest density, a rather weak variation with density is observed in the measurement. This is keeping with the density independent prediction for the plateau regime.

A more limited version of this data is available for the Mirror configuration, as illustrated in figure 7.23. The biased electrode was fixed at  $r/a \sim 0.7$  and the Mach probe at  $r/a \sim 0.86$ . The trend in this data is similar to the QHS data presented in the previous graph, and confirms the prediction of a limited variation of the slow rise time scale with density. Note that in both the radial profile at fixed density and the density scan at fixed radial location, the model tends to slightly underestimate the measured rate for the Mirror configuration.

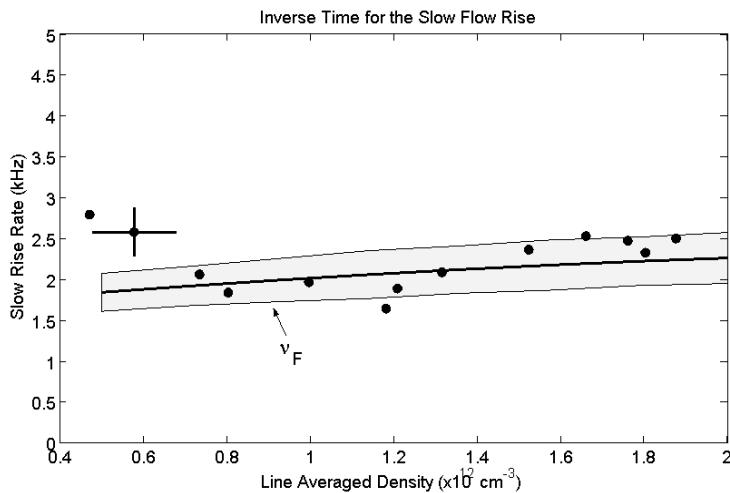


**Figure 7.22: Comparison between the measured slow rise inverse time scales and the modeled rise rate  $v_F$  as a function of density, for the QHS configuration of HSX.**

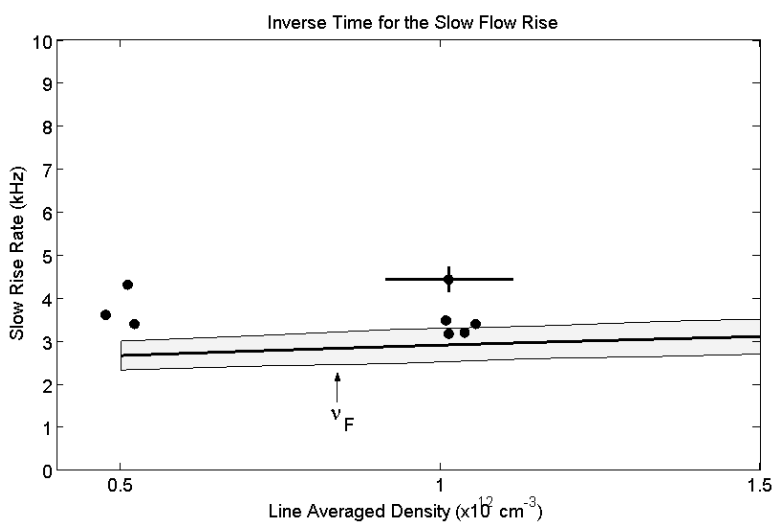


**Figure 7.23: Comparison between the measured slow rise inverse time scales and the modeled rise rate  $v_F$  as a function of density, for the Mirror configuration of HSX.**

### 7.2.3 Flow Directions Associated with the Flow Rise.

As repeated in the introduction to this section, the prediction from the spin-up model is that the flow will grow on a fast time scale in the covariant poloidal direction, followed by a slower evolution in the parallel direction on the hybrid time scale  $v_F$ . The magnitude of these time scales

has been verified in the previous two sections, and what remains is a test of the directions themselves.

As noted in Section 4.4, the fit to the flow rise often has difficulty in determining the direction and time scale associated with the fast flow, especially in the QHS configuration. More precisely, the fast direction converged to by the fit is not always the same as the direction in which the initial growth of the flow occurs. In general, the Mach probes are not capable of making measurements of events which happen on this  $<20\mu\text{s}$  time scale. When the direction associated with the fast flow is incorrect, it can cause there to be an error in the direction associated with the slower flow rise.

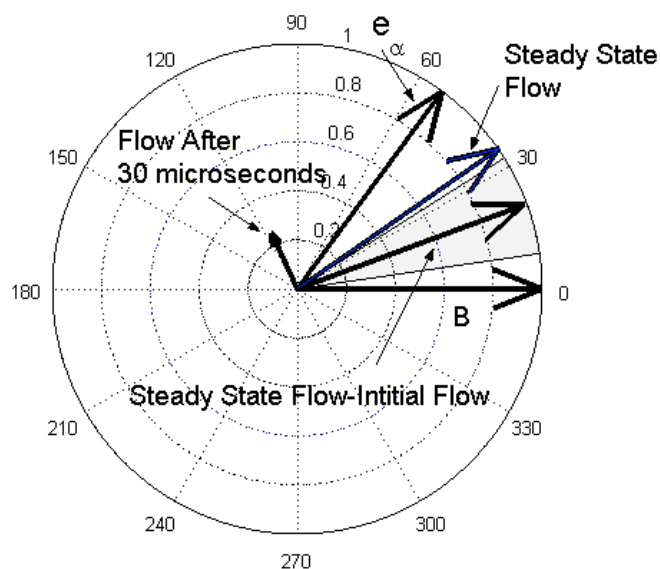


**Figure 7.24: Predicted and measured directions associated with the spin-up as measured by the low field side Mach probe in the QHS configuration.**

To overcome these limitations on the fits, we will use a slightly different technique to determine the directions associated with the flow evolution. Call  $U_1$  the approximately parallel flow and  $U_2$  the flow in the surface but approximately perpendicular to the magnetic field, as per the definitions used in Section 4.4. Noting that the fast flows grows with a time scale of  $\sim 1-10\mu\text{s}$  and the slow flow on a time scale of  $100-400\mu\text{s}$ , it is possible to define the flow direction after fast flow evolution as  $U_{1f}=U_1(t=30\mu\text{s})$  and  $U_{2f}=U_2(t=30\mu\text{s})$ . With the definition that  $U_{1ss}$  and  $U_{2ss}$  are the

steady state values of the flow, the directions associated with the slower flow evolution ( $U_{2s}$  and  $U_{2s}$ ) can be determined as  $U_{1s}=U_{1ss}-U_{1f}$  and  $U_{2s}=U_{2ss}-U_{2f}$ .

An example of these comparisons is shown in figure 7.24, for a  $1 \times 10^{12} \text{ cm}^{-3}$  plasma in the QHS configuration, with the Mach probe located at  $r/a \sim 0.90$ . The flow arrows have been normalized in this and similar figures so that the steady state flow has a magnitude of 1. Consider the arrows starting from the left. This arrow represents the flow speed  $30 \mu\text{s}$  after the electrode voltage is applied. This direction should, according to neoclassical theory, be compared to the vector  $\mathbf{e}_\alpha$ , which has been normalized to unit length in this figure. In principle, these vectors should point in the same direction. On the other hand, it should be remembered that the flow is changing very quickly during this time and is difficult to accurately measure.

Continuing clockwise around the graph, the next arrow reached is the measured steady state flow direction. This is the direction that was discussed previously in Section 7.1.3. The difference between the fast flow direction and the steady state must be the slow flow direction, which is the next arrow in the clockwise direction. The error region surrounding the slow flow is representative of the systematic alignment error with respect to the field, and should be included for all three measured directions. Note that the vector sum of the slow flow and fast flow directions is equal to the steady state flow. The slow flow direction should, according to the model, be aligned with the parallel direction, which is the final arrow in the plot. This does not seem to be exactly the case.

The time  $30 \mu\text{s}$  was chosen in this graph to select the fast flow direction. Picking various different values of this time ( $15-40 \mu\text{s}$ ) leads to somewhat different values of the fast direction. On the other hand, because there is more slow flow than fast flow in the QHS case, changes in the fast direction do not have a large impact on the slow direction. It is for this reason that the slow time scale can be extracted from the data with reasonable accuracy despite the inability to resolve the details of the faster time scale.

With these caveats in mind, it appears that in general, the slower flow rise direction is  $\sim 15^\circ$ - $20^\circ$  displaced from the parallel direction in the poloidal-toroidal plane. This could in principle be due to a error in the angle calibration of the probes. On the other hand, flow damping terms not included in the modeling could lead to modifications of the various directions. A more sophisticated model of the spin-up, including some surface to surface connection and proper understanding of the electric field formation process, is necessary to properly resolve these issues.

The picture displayed for the low field side probe is approximately the same for the high field side probe. An example measurement is shown in figure 7.25. This data is for the QHS configuration, and the HFS Mach probe is located at  $r/a \sim 0.9$ . Note that compared to the previous plot, the direction of the vector  $\mathbf{e}_\alpha$  is significantly changed with respect to the direction of the field. As explained in Chapter 5, this flip in  $\mathbf{e}_\alpha$  essentially represents the reversal of the Pfirsch-Schlueter current when measured on the outboard side at low and high field locations.

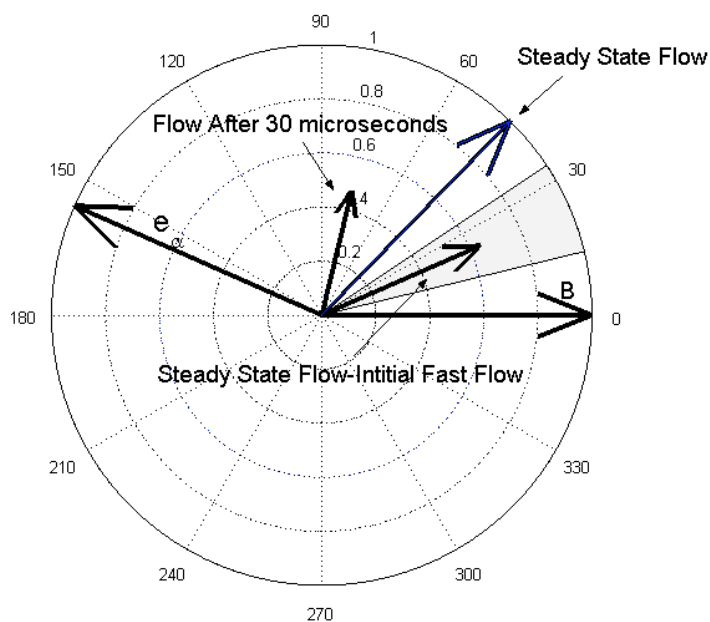


**Figure 7.25: Predicted and measured directions associated with the spin-up as measured by the high field side Mach probe in the QHS configuration.**

As with the previous figure, the fast flow (at 30  $\mu$ s) and the slow flow add up to the steady state flow. As before, the slow flow direction, which should be in the parallel direction, is rotated somewhat counterclockwise of the field direction. There is a large discrepancy in the fast flow directions, but this "error" should be taken with some caution for the reasons described above.

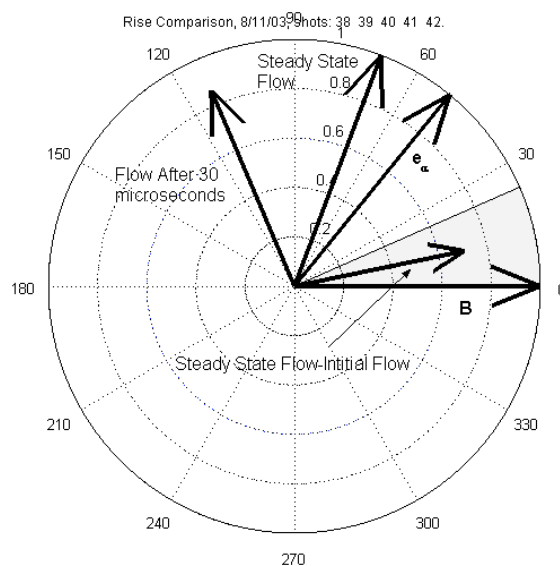


**Figure 7.26: Predicted and measured directions associated with the spin-up as measured by the low field side Mach probe in the Mirror configuration.**

These sorts of comparisons can be made for the Mirror configuration as well. The graph in figure 7.26 shows a comparison of the measured steady state and flow rise directions in the Mirror configuration. The measurement is made at  $r/a=0.95$ , using the low field side Mach probe in a discharge with a line average density of  $1 \times 10^{12} \text{ cm}^{-3}$ . This graph is similar to the QHS case in figure 7.24, but with a few subtle differences. The steady state flow is rotated farther in the counterclockwise direction for the Mirror case compared to the QHS. This corresponds to a rotation of the flow vector away from the direction of symmetry, as expected with the larger toroidal viscosity. The experimental reason for the rotation of the flow direction compared to the QHS case is that a larger fraction of the total flow appears in the direction of fast flow rise. The direction associated with the slower flow rise is nearly parallel to the magnetic field, as expected from the modeling. As a side note, because there is more flow associated with the fast direction in

the Mirror configuration, the two time scale fits tend to work better there than in the QHS configuration.

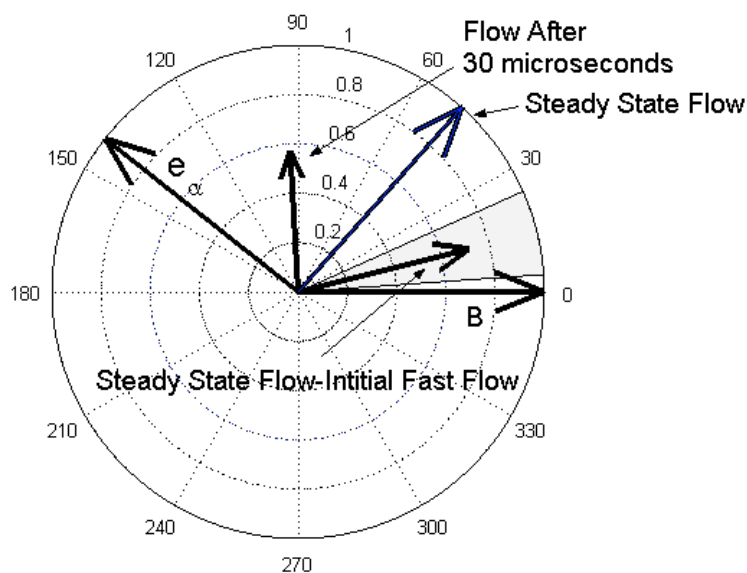


**Figure 7.27: Predicted and measured directions associated with the spin-up as measured by the high field side Mach probe in the Mirror configuration.**

For completeness sake, the spin-up directions for the Mirror configuration on the high field side are illustrated in figure 7.27. The data looks very similar to that measured on the HFS in the QHS configuration, although the slow flow rise direction is somewhat closer to the parallel direction.

Concerning radial profiles of the fast and slow directions, the graphs in figure 7.24, 7.25, 7.26, and 7.27 are generally valid for all radial locations along the line of the probe. No strong variation with radius is observed. These figures are sufficient to summarize the findings with respect to the flow directions.

## 7.2.4 Summary

This section has summarized the comparison between the measured and modeled flow spin-up and electric field rise. The modeling implicitly predicts the electric field formation correctly, and correctly predicts the observed spike in the electrode current. The model correctly predicts the radial profile and density scaling of the time scale for the slowly evolving flow. The direction of the slowly evolving flow appears to be somewhat different than the prediction, for both the high and low field side measurement probes. Generally speaking, the model appears to encapsulate many of the features of the plasma spin-up correctly, but some discrepancies remain. Further modeling, including a more detailed treatment of the surface to surface connection and a proper treatment of the fastest time scale, might resolve some of these issues.

## 7.3: Comparison between the Plasma Flow and Floating Potential Decay Measurements and Neoclassical Modeling

The final step is to compare the measured decay in the plasma quantities with the modeling predictions. Recall that the neoclassical flow decay model, derived from the formulation by Coronado and Talmadge, was based upon or implied the following:

- 1: The electrode (external) current is terminated very quickly at the end of the bias pulse. This occurs faster than any of the plasma time scales.
- 2: The electric field decays with two time scales.
- 3: The plasma flow decays with two time scales and two directions. Both of these time scales are determined by the magnetic field geometry and the plasma parameters.
- 4: The slower flow decay rate should correspond to flow in the direction of symmetry.

The electrode current is observed to turn off on a time scale of  $\sim 1\mu\text{s}$ , as will be shown below. This is faster than either of the neoclassical time scales or the particle and energy confinement time scales, and thus point 1 above is satisfied. The remaining three points will be

discussed in more detail below. Before continuing, it is suggested that the reader review the discussion of the flow decay fits in Section 4.4.2.

### 7.3.1 Radial Profiles of Plasma Flow and Potential Relaxation Parameters

To begin the study, consider a comparison between the neoclassical fast time scale and the time scale for the electric fields and potentials to decay. This data was taken in the QHS configuration with a line average density of  $1 \times 10^{12} \text{ cm}^{-3}$  and  $\sim 350 \text{ V}$  on the electrode during bias. The proud pin of the Mach probe was used to monitor the profile of the floating potential evolution. The profiles of the inverse decay time for the floating potential are shown as solid symbols in figure 7.28. Diamonds correspond to measurements taken on the high field side of the machine, while squares correspond to measurements from the low field side. As noted before, the measurements from the two locations agree quite well. The profile of the inverse decay time is fairly flat inside of  $r/a=0.9$ , showing that the electric field uniformly collapses inside that radius after the electrode current is broken.

This figure also shows the inverse decay time of the electrode voltage as open symbols. The electrode was held at a fixed location for these experiments; the data is presented as a function of the Mach probe location. The electrode voltage inverse decay time does not change as the Mach probes are moved, implying that the Mach probes are not overly perturbative, at least for this quantity.

Note that this time scale for the voltage to decay from the electrode is not determined by the power supply. As discussed in Section 2.1, the power supply has a capacitance of  $\sim 70 \text{ nF}$  due to the snubbing capacitors. Using a plasma impedance of  $\sim 50 \Omega$ , the time scale for the decay would be about  $RC=3.5 \mu\text{s}$ . The observed time scale is approximately 10 times larger than this.

The fast time scale from the Coronado and Talmadge model is shown in figure 7.28 as well. It appears that the decay time scales for these electric field quantities are well described by the fast Coronado and Talmadge time scale, except for the last 10% of the minor radius.

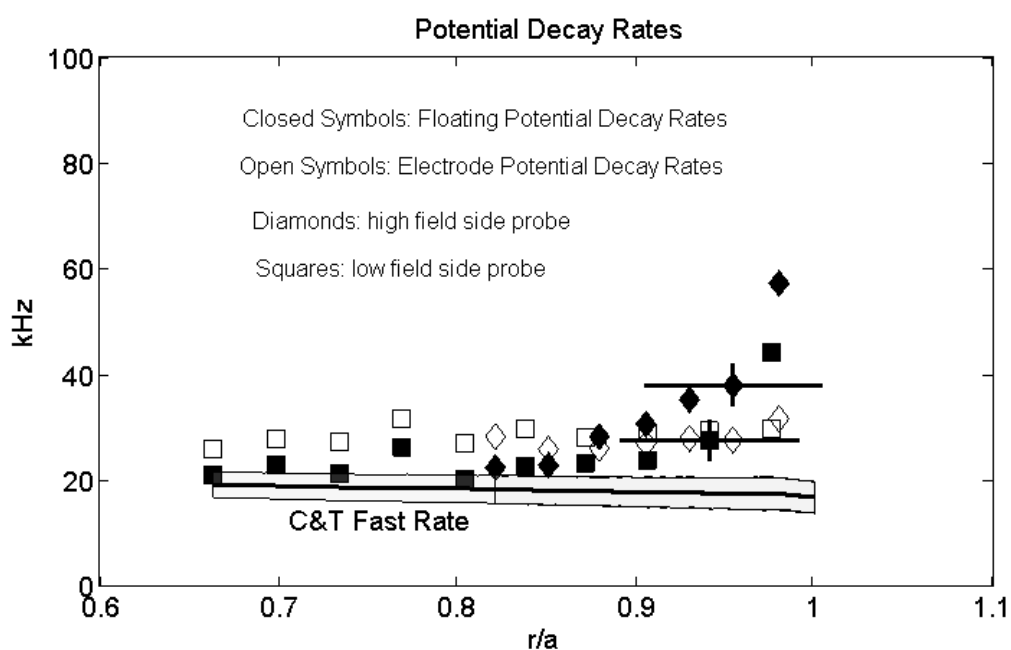


Figure 7.28: The inverse decay time for the electrode and floating potentials for the QHS configuration. Diamonds correspond to measurements taken on the high field side, while the squares are for measurements on the low field side. The Coronado and Talmadge fast neoclassical rate is also shown.

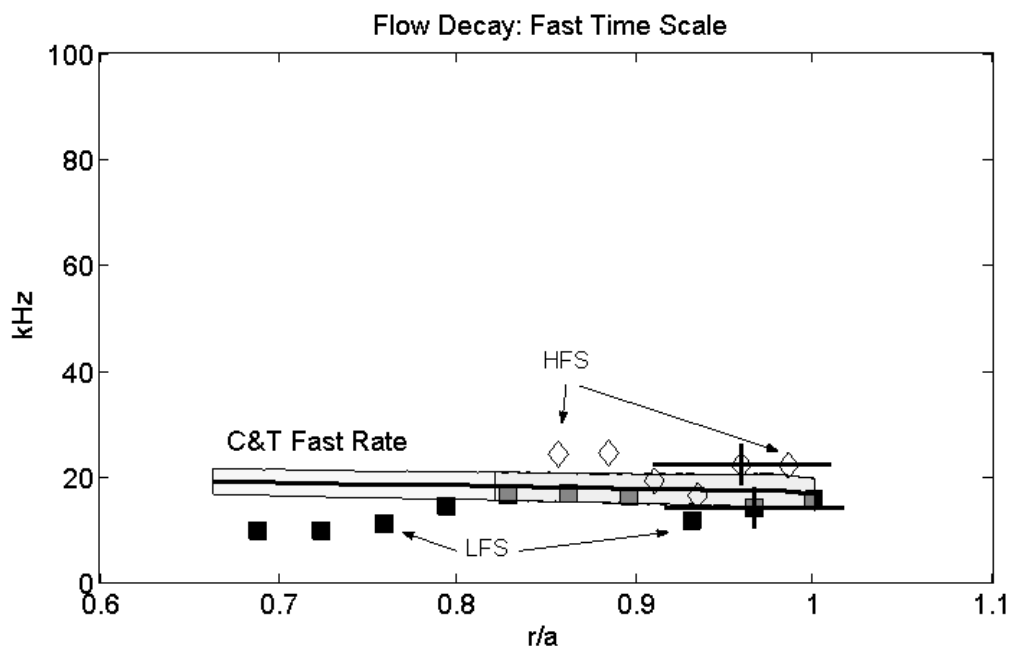
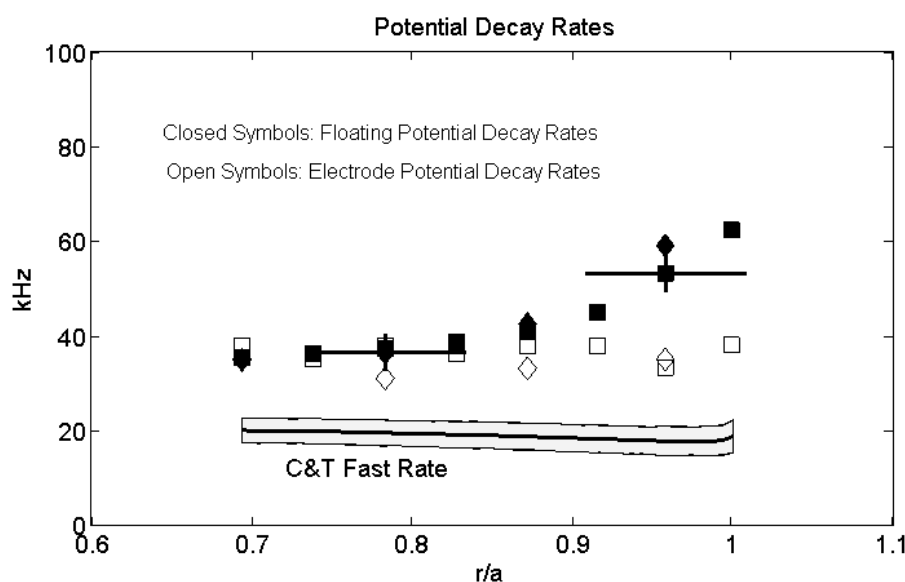


Figure 7.29: Comparison of the QHS configuration inverse time scale for the fast flow decay and the Coronado and Talmadge fast time scale.

The inverse decay time of the fast flow is shown in figure 7.29, for the same discharges as in the previous figure. There are a number of points to take away from this graph. As with other measurements, time scales measured on the low and high field sides are quite comparable (diamonds for HFS, squares for LFS). The time scales for the fast flow decay and the floating potential decay are also quite similar, as can be seen by comparing this and the previous figure. The fast flow decay time scale is in approximate agreement with the Coronado and Talmadge fast time scale.



**Figure 7.30: Comparison of the Mirror configuration floating potential and electrode potential decay rates to the Coronado and Talmadge fast rate. The different shaped symbols represent data taken on different days.**

A similar set of measurements has been made in the Mirror configuration of HSX. These discharges had a line average density of  $1 \times 10^{12} \text{ cm}^{-3}$ , with  $\approx 350 \text{ V}$  on the electrode during bias. These potential decay measurements are displayed in figure 7.30 and are to be interpreted as in figure 7.28 one for the QHS configuration. The plot shows the inverse decay time of the floating potential as a function of the Mach probe position. Measurements from two different days show good agreement, indicating the reproducibility. The electrode voltage decay time is shown as well, as a function of the Mach probe locations. The Mach probe position does not appear to

impact the rate at which the electrode floating potential decays, in the Mirror configuration as well as the QHS case. The potentials appear to decay somewhat faster in the Mirror configuration than in the QHS, as noted in Section 4.5 and can be inferred comparing figures 7.28 and 7.30.

The inverse decay time for the fast flow component in the Mirror configuration is shown in figure 7.31. The times agree reasonably well with the neoclassical fast time scale.

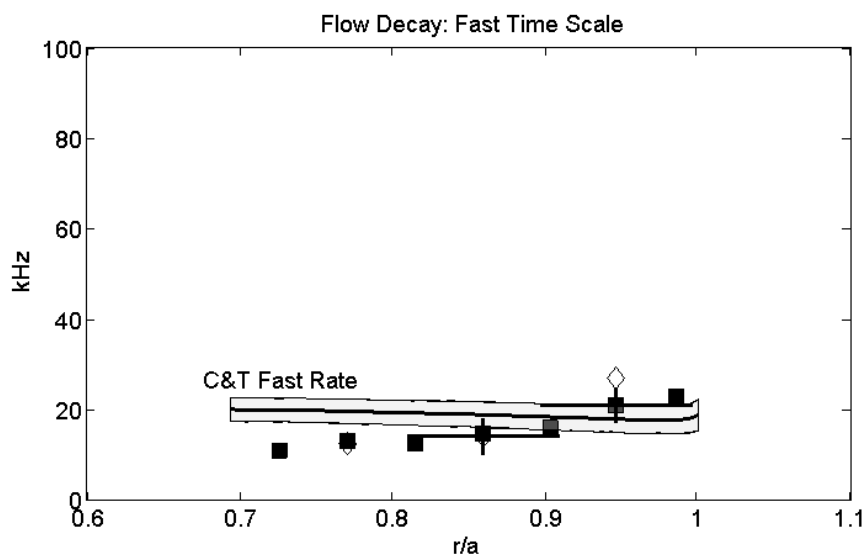


**Figure 7.31: Comparison of the Mirror configuration fast flow decay rates to the fast rate and the neoclassical fast rate. The two symbols correspond to data taken on two different days.**

While this data may seem totally consistent with the neoclassical modeling, there is an important caveat to be noted. The neoclassical modeling predicts that the electric field will decay with *two* time scales. The measured floating potential decay only displays one time scale, as shown in figure 4.24. This time scale appears to be consistent with the Coronado and Talmadge fast time scale. On the other hand, the lack of a slow time scale evolution in the floating potential illustrates that the neoclassical picture of the electric field decay is not entirely consistent with the data.

As a further emphasis on this point, the agreement between the inverse time scale for slow flow decay and the Coronado and Talmadge slow time scale is quite poor. The measured inverse

time scale for slow flow decay is shown in figure 7.32. Data from both high and low field side Mach probes are included in this comparison. The slow time scale from the Coronado and Talmadge model is also shown in the figure. This rate is mainly determined by the ion-neutral collision frequency ( $\langle\sigma v\rangle_{cx}\sim 10^{-8}T_i^{.318}$ , so  $v_{in}=n_n\langle\sigma v\rangle_{cx}\sim 1\times 10^{10}10^{-8}20^{.318}\sim 250$  1/s)<sup>12</sup> The flows are damped more quickly than the neoclassical prediction by a factor of  $\sim 10$ . This measurement, in addition to the radial conductivity measurements in 7.1.1 and 7.1.2, provides reason to believe that momentum damping in the symmetry direction is dominated by some non-neoclassical effect, as in a tokamak.

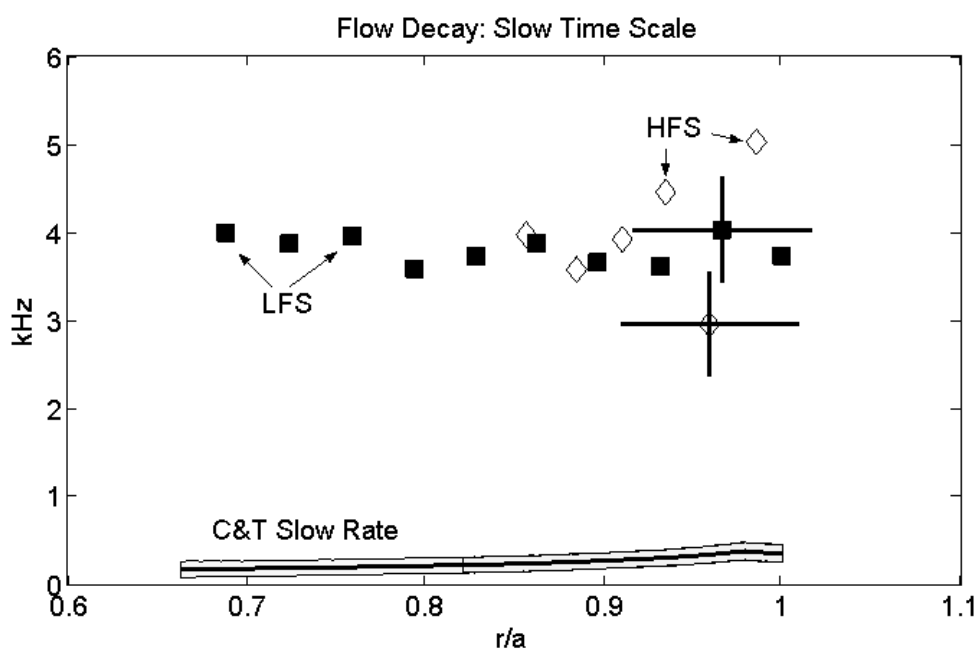


**Figure 7.32: Comparison between the measured and modeled inverse time scales for slow flow decay for the QHS configuration. Data from the high and low field side Mach probes is displayed.**

These measurements have been made in the Mirror configuration as well, as shown in figure 7.33. The two different symbols represent two days with identical plasmas, indicating the reproducibility of the data. Simultaneous high and low field side measurements (not shown) also show similar time scales. The measured slow decay inverse time scale is approximately two times larger than the QHS case, as was first shown in Section 4.5. The neoclassical prediction is

approximately 4 times larger than that for the QHS case, due to the large increase in the non-symmetric field ripple. Hence, the discrepancy between the Mirror modeling and measurements is approximately a factor of 3 to 4. Once again, the Mirror configuration modeling, with its larger neoclassical viscous damping of flows, agrees more closely with the measurements than the modeling for the QHS configuration.

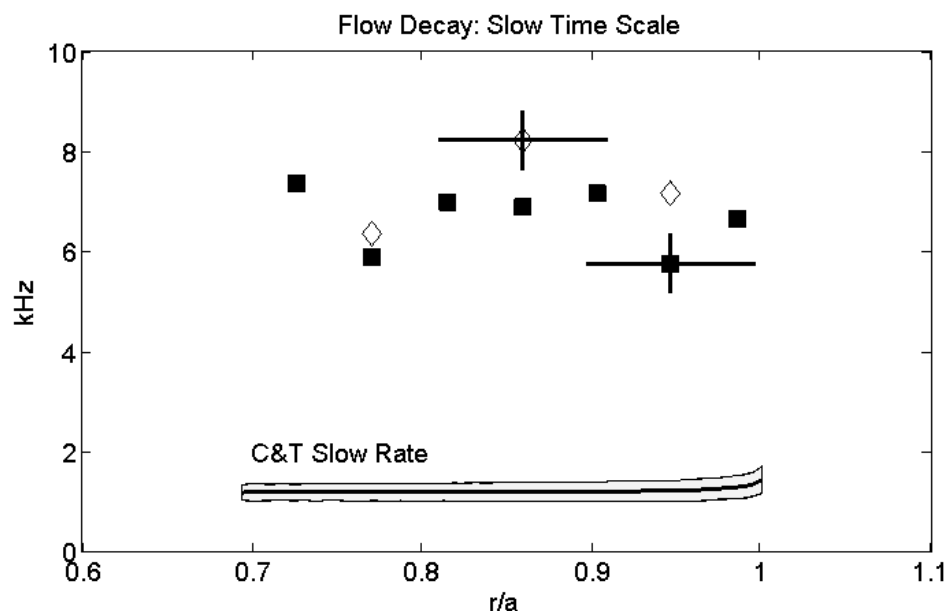


**Figure 7.33: Comparison between the measured slow decay inverse time scales for the Mirror configuration. Different symbols correspond to two days of identical plasma.**

At this point, it is worth explicitly showing that the momentum transport is not classical. To derive a simple classical scaling, consider a simplified momentum equation of the form<sup>13</sup>

$$\rho \frac{\partial V}{\partial t} = \rho \nu_{\perp} \nabla^2 V$$

where  $\rho$  is the mass density,  $V$  is the flow velocity, and  $\nu_{\perp}$  is the kinematic viscosity. The classical kinematic viscosity is of order  $\nu_{\perp} \sim \rho_i^2 \nu_i$ . Using  $\rho_i \sim .001\text{m}$  and the NRL formulary expression  $\nu_i = 4.8 \times 10^{-8} \cdot 7 \times 10^{11} \cdot 15 \cdot 20^{-3/2} \sim 5500 \text{ 1/s}$ , the kinematic viscosity becomes  $\nu_{\perp} \sim .005 \text{ m}^2/\text{s}$ . Using this expression to define a diffusive slowing down time yields  $\tau_{SD} \sim (\Delta r)^2 / \nu_{\perp} \sim 0.2 \text{ s}$ . This is approximately two orders of magnitude too slow to explain the measured flow damping. On the other hand, the slow flow decay time of  $\sim .3\text{ms}$  is not so dissimilar to the energy confinement time of  $\sim 1\text{msec}$ .

### 7.3.2 Density Scaling of Plasma Flow and Potential Relaxation Parameters

Consider next the variation of the decay times with density. The inverse times for the decay of the electrode voltage and current are illustrated in figure 7.34. These plots are for the QHS configuration. In these discharges, the electrode was held fixed at  $r/a \approx 0.65$  and the Mach probes held at  $r/a \approx 0.8$  while the density was adjusted shot to shot via the gas feed. The decay time for each individual bias pulse is illustrated, so there are 6 pulses/discharge x 35 discharges = 210 data points in this figure.

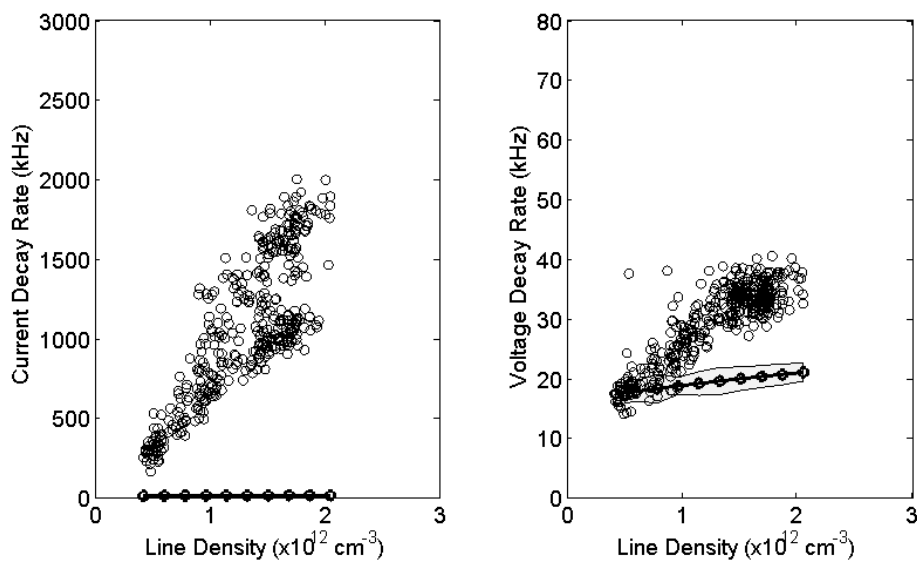


**Figure 7.34: Comparison between the electrode current (left) and voltage (right) inverse decay times as a function of density in the QHS configuration, as well as the Coronado and Talmadge fast time scale. Note the different vertical scales.**

The inverse decay time of the electrode current (left frame of figure 7.34) is much faster than either the electrode voltage inverse decay time or the Coronado and Talmadge fast rate. It is also substantially faster than energy and particle confinement times, which are  $\sim 1$ ms. These observations are in keeping with the assumptions of the modeling, where it is postulated that the electrode current is shut off instantaneously.

The inverse decay time of the electrode voltage is shown in the right hand frame of figure 7.34. As noted before, the inverse decay time for the electrode voltage is very similar to the Coronado and Talmadge fast rate. The magnitudes are within a factor of two of the neoclassical prediction for all densities. The measured variation with density is similar to, but somewhat stronger than, the neoclassical prediction

Further comparisons regarding the density scaling of fast decay quantities are shown in figure 7.35. Discharges with identical probe locations and similar densities have been averaged to produce this figure. The inverse times for the decay of the floating potential and the electrode voltage are shown in the left frame of the figure. The Mach probe was located at a larger minor ( $r/a=0.8$ ) radius than the electrode ( $r/a=0.65$ ), and the floating potential at its location decays faster. This is consistent with the radial profiles presented above. The Coronado and Talmadge fast time scale is included in the plot as well, and matches the data reasonably well.

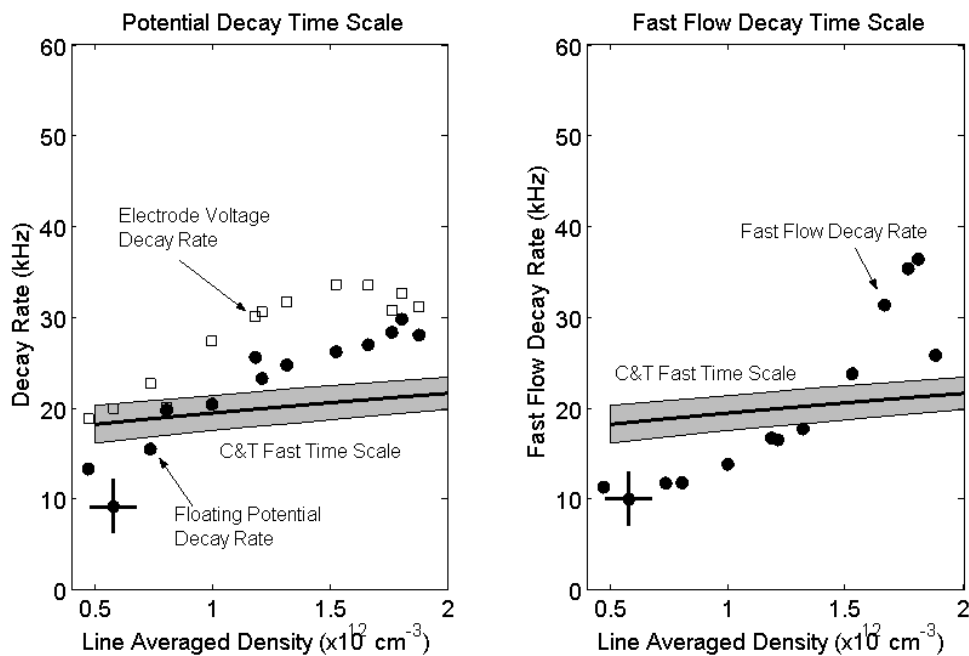


**Figure 7.35: Comparison between the electrode and Mach probe floating potential decay rates and the fast Coronado and Talmadge time scale (left). Comparison between the fast flow decay rate and the Coronado and Talmadge fast time scale (right).**

The inverse time scale for the fast component of the flow decay is shown on the right in this figure. The rate at which the fast component of the flow decays is in reasonable numerical agreement with the neoclassical predicted fast time scale, though the density scaling is stronger than predicted by the modeling.

In general, these figures illustrates that 1) the electrode voltage, floating potential and fast component of the flow all decay on similar time scales, 2) all of these quantities have the same trend vs. minor radius, 3) this time scale is very similar to the fast time scale from the Coronado and Talmadge modeling, and 4) the measured time scales show a scaling with density which is similar to, but somewhat stronger than, the scaling predicted by the aforementioned model.

The final comparison of the density scaling is between the measured inverse time for the slower flow decay and the neoclassical slow time scale. This comparison is shown in figure 7.36. The measurements were made with the LFS Mach probe in the QHS configuration. The slow decay rate decreases as the density is increased, in contrast to the neoclassical modeling. While it appears that the two curves are coming together at the highest density, the slow flow damping is still anomalous.

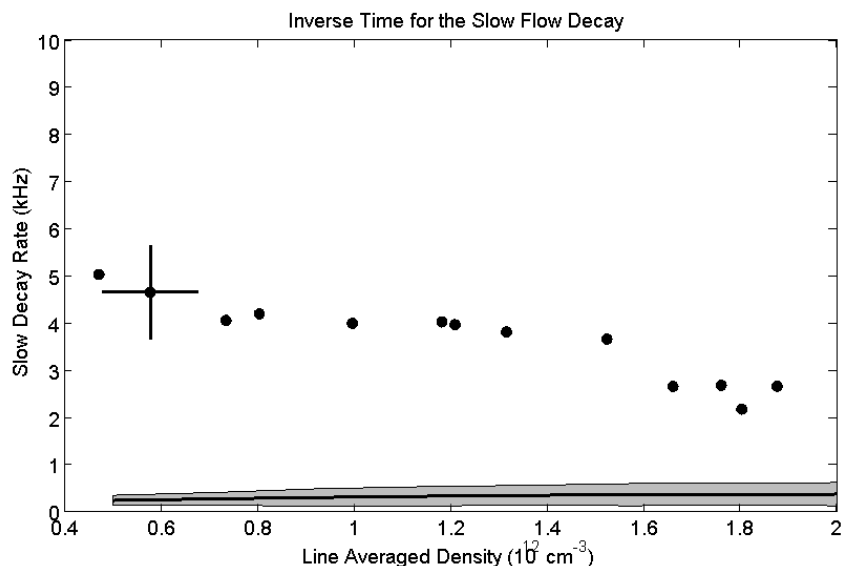


**Figure 7.36: Comparison between the measured inverse decay rate of the slow flow component and the calculated Coronado and Talmadge slow time scale.**

The neoclassical slow time scale is dominated by the ion neutral collision frequency. The increase of the modeled slow damping rate is due to the increase in the neutral density when the plasma density is raised. To review this point, the gas puff is increased to achieve higher density in HSX. As the density is increased, the screening of the  $H_2$  is improved. The ionization of these  $H_2$  molecules provides the majority of the particle source according to DEGAS calculation. On the other hand, the screening of the H atoms is still insufficient to keep the atoms from moving freely throughout the plasma. Hence, over the range of densities that HSX operates at, raising the plasma density by gas puffing results in an increase in the neutral atom density.

### 7.3.3: Flow Decay Directions

The anomalously fast decay of the flow is coupled to somewhat inexplicable behavior in the flow decay directions. Recall from Section 4.4.2 that the flow decay is analyzed using a two time scale/two direction fit approach. The fit parameters  $C_1$ ,  $C_3$ ,  $C_4$  and  $C_6$  in equation 4.4 described the directions and magnitudes of the flow decay, and are the basis of the comparisons in this section. These fits were shown to be only marginally successful in describing the flow evolution.

The polar plot in left frame of figure 7.37 illustrates the directions associated with the fast and slow flow decays. The data shown is for the QHS configuration, with a line average density of  $1 \times 10^{12}$ . The Mach probe is on the low field side, at  $r/a \sim 0.93$ . One component of the flow decays on a time scale similar to the floating potential decay time. The direction associated with this decay is shown in the left frame as the direction of fast flow decay. The remaining flow, which decays on the slower time scale, appears to be mostly in the parallel direction. This picture is self consistent, in the sense that the parallel flow will not cause any electric field. The steady state flow is shown in the figure, and note that the fast and slow flow decays sum to the steady state flow. This picture is representative of the observations at other densities and in the Mirror configuration.

The picture is not consistent with the neoclassical picture of flow decay, as described near figure 6.6 and repeated in the right hand frame of figure 7.37. The orientation of the coordinate system is the same in both figures, and they have been separated from each other for the sake of clarity only. The steady state flow is to the counterclockwise of the neoclassical prediction, as noted in figure 7.13. The modeled and measured slow and fast decay directions are not at all similar.

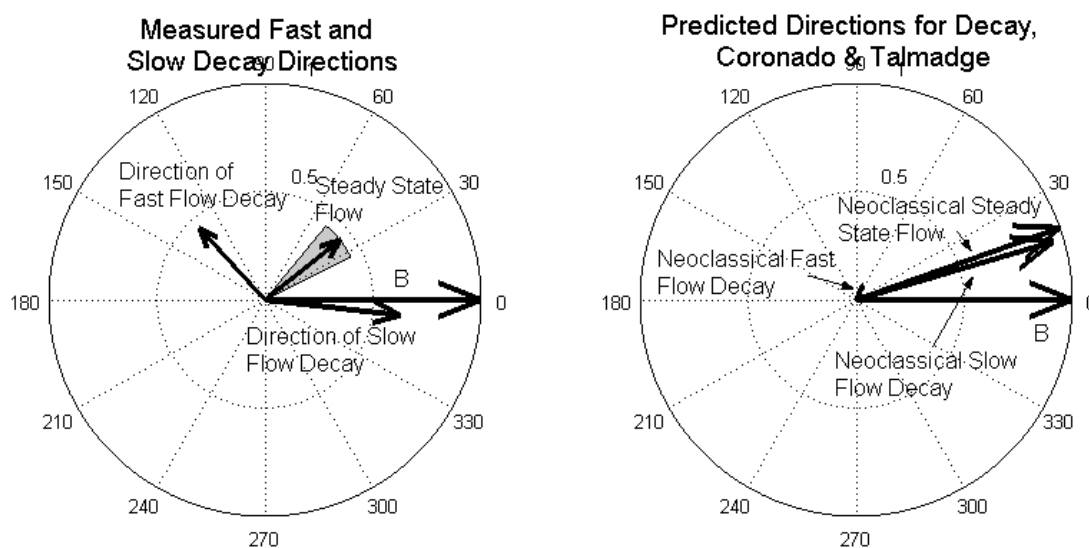


**Figure 7.37: Measured directions associated with the flow decay (left) and the neoclassical prediction (right), for the LFS in the QHS configuration. Both figures are aligned with the magnetic field pointing to the right, but the radial scale is arbitrary.**

The caveat from Section 4.4 bears repeating at this juncture. The two time scale/two direction fit was often a very poor model for the observed flow relaxation behavior. The directions illustrated in figure 7.37 are of dubious physical meaning. The most significant conclusion to be taken from this picture is that the decay is not in keeping with the neoclassical prediction.

### 7.3.4: Summary

This section has provided detailed comparisons between the measured and modeled flow and potential relaxation. The model predicts a fast time scale for a portion of the flow and electric field to decay. The measured decay of the electrode voltage, floating potential, and the

fast component of the flow all decay on this time scale. On the other hand, the slow decaying component of the flow decays more quickly than the neoclassical prediction, and there is no sign of the slow time scale in the floating potential decay. The fast and slow flow decay directions, to the extent that they can be resolved, are not those predicted by neoclassical theory. In this sense, it has been concluded that there is some anomalous damping of plasma flows in HSX.

## 7.4 Discussion and Summary

A detailed comparison between neoclassical damping predictions and measurements has been presented in this chapter. Many observations have been made, and a minimal statement of observations might be:

- 1: The radial conductivity in HSX is anomalously large. It cannot be explained by neoclassical theory including the effects of neutrals.
- 2: A model which predicts the radial conductivity in L-mode tokamaks, where anomalous momentum damping is widely believed to take place, is roughly consistent with the HSX measurements.
- 2: The measurements of the plasma spin-up are approximately consistent with the model presented in Chapter 6. This model shows that the flow growth should occur at a rate substantially faster than the slowest neoclassical flow damping rate.
- 3: The measured fast decay rates (for potential and flow) are approximately consistent with the neoclassical prediction.
- 4: The slow decay rates predicted by neoclassical theory are not observed in the data. The slower decay of the flow is  $\sim 10$  times faster than predicted, and there is no slow decay observed in the floating potential.
- 5: The directions associated with the slow and fast flow decay cannot be explained using neoclassical theory.

Synthesizing these observations would lead to the following rather general conclusions. Phenomena associated with the neoclassical fast time scales, such as the damping of flows across the direction of symmetry, seem to be described reasonably well by neoclassical theory. Phenomena which have a strong dependence on the damping in the symmetry direction are not well described by neoclassical theory.

- 
- <sup>1</sup> V. Rozhansky, and M. Tendler, *Phys. Fluids B* **4**, 1878 (1992).
- <sup>2</sup> G. Greiger, et. al, *Plasma. Phys. Control. Fusion* **28**, 43 (1986)
- <sup>3</sup> J.N. Talmadge, B.J. Peterson, D.T. Anderson, F.S.B. Anderson, H. Dahi, J.L. Shohet, M. Coronado, K.C. Shaing, et. al., *Proceedings of the 15<sup>th</sup> International Conference on Plasma Physics and Controlled Fusion Research (Seville, 1994)*, IAEA, Vienna, **1** (1995) 797.
- <sup>4</sup> L.G. Askinazi, V.E. Golant, S.V. Lebedev, V.A. Rozhanskij, and M. Tendler, *Nuclear Fusion* **32**, 271 (1992).
- <sup>5</sup> Personal communication with J.N. Talmadge
- <sup>6</sup> M. Coronado and J. Galindo Trejo, *Phys. Fluids B* **2**, 530 (1990).
- <sup>7</sup> M. Okabayashi and S. Yoshikawa, *Phys. Rev. Lett.* **29**, 1725 (1972).
- <sup>8</sup> M. Coronado and J. N. Talmadge, *Phys. Fluids B* **5**, 1200 (1993).
- <sup>9</sup> Personal communication with J.M. Canik.
- <sup>10</sup> Heifetz, D.B. et. al., *J. Comp. Phys.* **46**, 309 (1982).
- <sup>11</sup> J. Canik, D.T. Anderson, S.P. Gerhardt, and J.N. Talmadge, *Proceedings of the 14<sup>th</sup> Stellarator Workshop*, Greifswald, Germany, 2003.
- <sup>12</sup> J. Cornelis, R. Sporcken, G. Van Oost, and R.R. Weynants, *Nuclear Fusion* **34**, 171 (1994).
- <sup>13</sup> A.F. Almagri, J.T. Chapman, C.S. Chaing, D. Craig, D.J. Den Hartog, C.C. Hegna, and S.C. Prager, *Phys. Plasmas* **5**, 3982 (1998).